RSC Advances

PAPER

View Article Online
View Journal | View Issue

Cite this: *RSC Adv.*, 2026, **16**, 21705

Design, synthesis, and enzyme kinetic evaluation of oxadiazole derivatives as nucleoside triphosphate diphosphohydrolase (NTPDase) inhibitors: an integrated *in vitro* and *in silico* approach

Syed Zaighum Abbas,[a] Zaman Ashraf,[*b] Sadia Roshan,[c] Kalsoom Sughra,[d] Muhammad Arslan Rahat,[e] Imran Shakir*[f] and Muhammad Latif *[bgh]

Given the pivotal function of ecto-nucleoside triphosphate diphosphohydrolases (ecto-NTPDases) in cancer progression and purinergic signaling, the identification of potential small heterocyclic inhibitors has become a significant objective in medicinal chemistry campaigns. This study concentrated on the development of substituted oxadiazole derivatives as ecto-NTPDase inhibitors. A series of 1,3,4-oxadiazole derivatives (**4**, **7a–7g**) were synthesized and assessed for their *in vitro* inhibition and *in silico* potential against ecto-NTPDases. *In silico* studies were conducted to predict pharmacokinetic properties using two different online tools, pkCSM and SwissADME. The results indicated favorable safety profiles with minimal or no toxicity and almost no pharmacokinetic violations. Molecular docking studies demonstrated that the 1,3,4-oxadiazole series selectively inhibited ecto-NTPDases with notable affinity toward NTPDase2, which is implicated in tumorigenesis and cancer progression. Structural interaction fingerprint (SIFt) analysis revealed that the binding affinities of the synthesized 1,3,4-oxadiazole derivatives with amino acid residues in the active binding site were higher than those of **Amp** and **Anp** redocked standards, which exhibited binding interactions with water molecules. Density functional theory (DFT) revealed the top docking hits and best inhibitors, further corroborating their stability and electronic suitability for enzyme inhibition. The successful synthesis of the target heterocycles was confirmed by FTIR and ^{1}H- and ^{13}C-NMR spectral analyses. Ecto-NTPDase inhibition and structure–activity relationship (SAR) studies indicated that **7g** was an excellent inhibitor of all isoforms, followed by **7d** and **7c** for NTPDase3 and NTPDase8, respectively. Kinetic inhibitory studies revealed that the best inhibitor, **7g**, exhibited non-competitive inhibition against NTPDase1 and 2 and mixed inhibition against NTPDase3 and 8. The Michaelis–Menten constants and inhibition constants of **7g** against NTPDase1 and 2 were K_m 0.028 μM, K_i 0.022 μM and K_m 0.02 μM, K_i 0.015 μM respectively. On the other hand, the inhibition constants of **7g** against NTPDase3 and 8 were K_i 1.13 μM and K_i 12.4 μM respectively. This study provides a robust foundation for the development of 1,3,4-oxadiazoles as potential inhibitors of ecto-NTPDases, particularly NTPDase2.

Received 21st February 2026
Accepted 17th April 2026

DOI: 10.1039/d6ra01543c

rsc.li/rsc-advances

[a]*Department of Chemistry, Allama Iqbal Open University, Islamabad, 44000, Pakistan. E-mail: realzagham@hotmail.com*

[b]*Department of Chemistry, Rawalpindi Women University, Rawalpindi, 46300, Pakistan. E-mail: zaman.ashraf@rwu.edu.pk*

[c]*Department of Zoology, University of Gujrat, Gujrat, 50700, Pakistan. E-mail: sadia.roshan@uog.edu.pk*

[d]*Department of Biochemistry and Biotechnology, University of Gujrat, Gujrat, 50700, Pakistan. E-mail: sughra@uog.edu.pk*

[e]*Department of Chemistry, University of Massachusetts, Amherst, Massachusetts, 01003, USA. E-mail: mrahat@umass.edu*

[f]*Department of Physics, Faculty of Science, Islamic University of Madinah, Madinah, 42351, Saudi Arabia. E-mail: imranskku@gmail.com*

[g]*Centre for Genetics and Inherited Diseases (CGID), Taibah University, Madinah, Saudi Arabia. E-mail: mmuradkhan@taibahu.edu.sa; Tel: +923484038134*

[h]*Department of Basic Medical Sciences, College of Medicine, Taibah University, Madinah, Saudi Arabia. E-mail: mmuradkhan@taibahu.edu.sa*

1. Introduction

Ecto-NTPDases, also known as ecto-adenosine triphosphatases (ecto-ATPases), are a group of enzymes with different types, like NTPDase1, 2, 3, and 8, which hydrolyze nucleosides such as adenosine triphosphate (ATP) and adenosine diphosphate (ADP). Generally, ATP is directly hydrolyzed to adenosine monophosphate (AMP), catalyzed by NTPDases,[1,2] but the presence of free ADP can be revealed upon hydrolysis of ATP by NTPDases 3 and 8.[3] Overexpression of NTPDase2 was observed in the brain, testis, and muscles, but occurred with a lower concentration in the lungs and liver during Northern blot analysis.[4] A similar pattern of overexpression of rat NTPDase2α has been observed in rats.[5,6] These reports were of profound

interest when cloning NTPDase2 DNA from a human carcinoma,[7] mouse hepatoma,[8] and human hepatoma Li-7A.[9] These results led to the conclusion that the upregulation of NTPDase2 results in tumor progression.

Several clinically used NTPDase inhibitors possess different side effects that limit their use. For instance, experimental investigations have shown that a clinically used ecto-NTPDase inhibitor, a nucleotide analog ARL 67156, caused a considerable increase in insulin release, even in the presence of a small quantity of glucose in the blood.[10] Oxadiazole derivatives, specifically 1,3,4-oxadiazoles, have attracted considerable attention in synthetic medicinal chemistry due to their wide range of pharmacological/biological activities.[11,12] These derivatives have been widely assessed for their therapeutic potential as anticancer,[13] anti-diabetic,[14] anti-microbial,[15] analgesic,[16] anti-inflammatory,[17] and anti-oxidant[18] properties. Due to their diverse bioactivity profiles and structural versatility, oxadiazole derivatives have emerged as ideal pharmacophores for the development of new potential agents. The importance of this pharmacophore is ascertained by the fact that many FDA-approved drugs, including raltegravir,[19] zibotentan,[13] tiodazosin,[20] butalamine,[21] and fenadiazole[22] have 1,3,4-oxadaziole ring.

Based on the therapeutic potential of 1,3,4-oxadiazole derivatives, we plan to synthesize substituted derivatives bearing this heterocyclic ring as potential inhibitors of NTPDase enzymes. In the present study, we synthesized 2,5-disubstituted 1,3,4-oxadizoles starting with methoxy-substituted benzoic acids *via* a facile reaction route. Inhibitory effects of the synthesized compounds were evaluated against ecto-NTPDase enzymes type 1, 2, 3, and 8. Furthermore, comprehensive computational studies were carried out to determine their binding affinities against target proteins. An *in silico* approach was also used to evaluate the cytotoxicity profiles of the synthesized derivatives.

2. Results and discussion

2.1. Chemistry

The compounds were synthesized by following already reported methods with slight modifications.[23,24] 1,3,4-Oxadiazole derivatives of 3,4-dimethoxybenzoic acid were synthesized through a multistep reaction process. Initially, 3,4-dimethoxybenzoic acid was refluxed with concentrated sulfuric acid in dry methanol to obtain methyl ester (**2**). In the second step, the desired ester (**2**) was refluxed with hydrazine hydrate to obtain hydrazide (**3**) in a good yield, which was refluxed with carbon disulfide (CS_2) and KOH to give 2-mercapto-1,3,4-oxadiazole (**4**). The CS_2 was slowly added in the reaction mixture at controlled temperature to avoid its loss and reaction yields has been improved. The pH of reaction mixture after completion of reaction was carefully adjusted as more addition of HCl decrease the pH which in turn protonated the oxadiazole ring nitrogen and intermediate **4** was not fully precipitated out. Finally, oxadiazole (**4**) reacted with *N*-substituted-α-bromo acetamide (**6a**), and benzyl halides (**6b–6g**) in the presence of potassium hydroxide in dry methanol to obtain substituted 1,3,4-oxadiazoles (**7a–7g**) in good yields (Scheme 1).

The peaks appearing in the FTIR, ^{1}H NMR, and ^{13}C NMR spectra revealed the coexistence of aromatic, aliphatic, and heteroatom-bonded environments. The moieties and

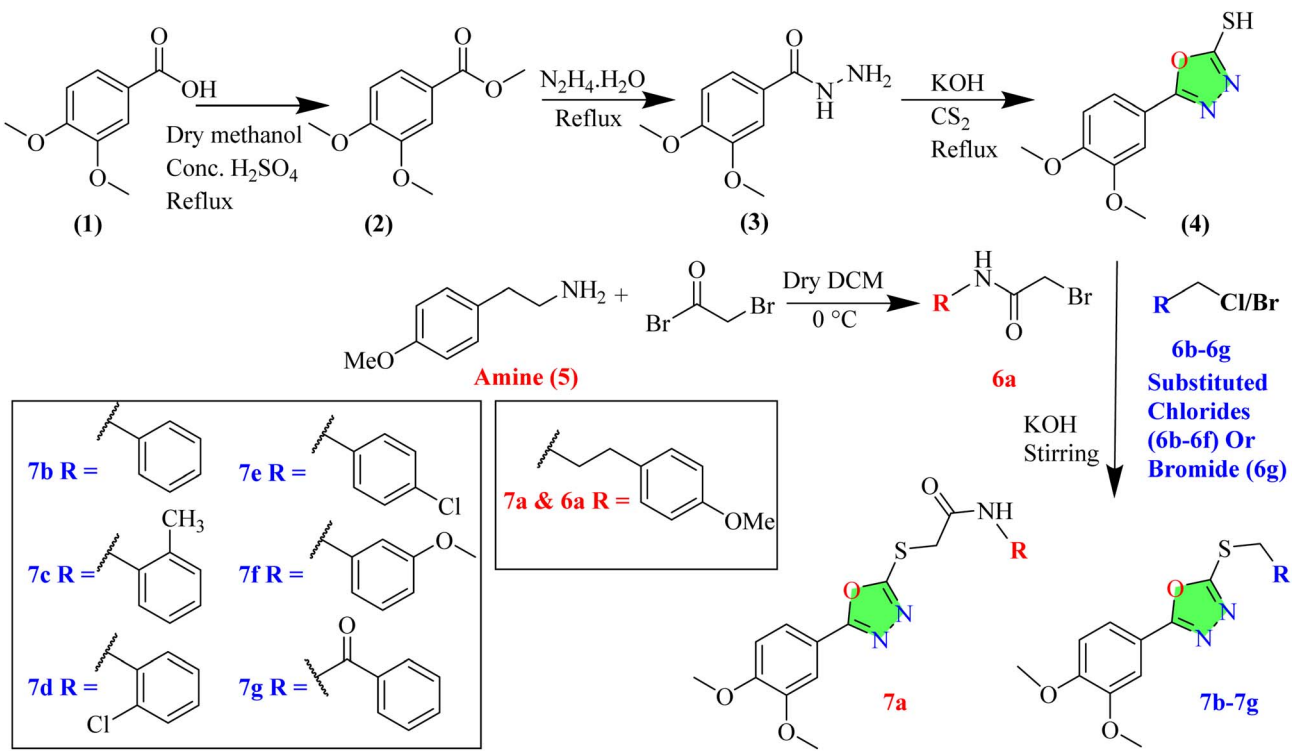

Scheme 1 Synthetic strategy for oxadiazole derivatives (**4**, **7a–7g**).

Table 1 Ecto-NTPDases inhibition of the synthesized 1,3,4-oxadiazoles (**4** and **7a–7g**)[a]

C. no	NTPDase1	NTPDase2	NTPDase3	NTPDase8
4	39.42 ± 1.87	NA	21.56 ± 1.32	64.62 ± 2.43
7a	NA	47.63 ± 2.09	45.26 ± 1.64	56.98 ± 2.06
7b	12.26 ± 0.91	23.43 ± 1.36	17.67 ± 1.41	36.39 ± 1.52
7c	19.45 ± 1.02	39.62 ± 1.93	8.28 ± 0.52	31.69 ± 1.37
7d	21.56 ± 1.08	17.73 ± 0.88	1.98 ± 0.14	29.58 ± 1.17
7e	65.23 ± 2.43	NA	NA	93.39 ± 3.82
7f	43.48 ± 1.58	32.65 ± 1.76	13.48 ± 0.92	49.62 ± 1.93
7g	5.13 ± 0.81	11.32 ± 0.56	1.21 ± 0.23	15.37 ± 1.08
Suramin	**16.1 ± 1.08**	**24.1 ± 0.95**	**4.30 ± 0.84**	**101.1 ± 2.34**

[a] IC_{50} ± SEM (standard errors of the mean) determined in triplicate, IC_{50} values were measured using PRISM 5.0 (GraphPad, California, USA) with *P*-value < 0.05 considering as statistically significant, (NA) not active.

functionalities present in oxadiazoles *i.e.* **4**, **7a–7g** resonated in their respective regions, with splitting patterns that confirmed the electronic characteristics of the substituents. The stretching absorptions (682–700 cm^{-1}) of C–S bonds in the FTIR spectra of (**7a–7g**) confirmed the formation of thioether linkages. In ^1H NMR spectra, peaks for aromatic protons were observed between 6.75–8.25 ppm, along with typical singlets for $-OCH_3$ protons between 3.50–4.00 ppm in (**4**, **7a–7g**). Presence of singlets at 3.50–5.50 ppm (**7a–7g**) in ^1H NMR spectra confirmed the formation of methylene bridge ($-CH_2-$). The formation of target oxadiazoles have also been ascertained by the presence of signals for methoxy C-atoms at 54–57 ppm and CH_2-carbons at 31–44 ppm as well as carbonyl carbons at 171.3 and 192.7 ppm in ^{13}C NMR spectra. The characteristic heterocyclic ring carbons and aromatic carbons appeared in their acceptable regions around 108–158 ppm confirmed successful synthesis of the target heterocycles. The FTIR spectrum of **7g** exhibited a characteristic absorption band at 1679 cm^{-1} which was attributed to the conjugated carbonyl (C=O) stretching vibration of the acetophenone moiety along with –OH absorption at 3343 cm^{-1}. The aromatic and aliphatic C–H stretching vibrations appeared in the range of 3072–2837 cm^{-1} and C–S stretching vibration appeared at 682 cm^{-1} confirmed the aliphatic C–S bond formation in **7g**. In ^1H NMR spectrum of **7g** the characteristic signal for methylene ($-CH_2-$) protons appeared as a singlet at δ 5.17, confirmed the successful formation of **7g** $-SCH_2-$ bridge in the final step of synthesis. The methoxy $-OCH_3$ protons also appeared as singlets at δ 3.82 integrating for six protons, supporting the presence of two equivalent $-OCH_3$ substituents. The acetophenone ring protons and 3,4-dimethoxyphenyl ring protons in **7g** resonated at aromatic regions δ 7.13 to 8.07 ppm. The signals appeared for methylene carbon ($-SCH_2-$) at δ 40.5 and $-OCH_3$ carbons at δ 55.6 in ^{13}C NMR spectrum were in full agreement with the proposed molecular structure of compound **7g**. A downfield signal at δ 192.7 was assigned to the carbonyl carbon of the acetophenone unit. The oxadiazole ring carbons appeared at δ 165.1 (C-1) and 162.5 (C-2), while aromatic carbons appeared in acceptable regions δ 108 to 151 ppm which confirmed synthesis of **7g**.

2.2.1. Ecto-NTPDases inhibition assay. The newly synthesized 1,3,4-oxadiazole derivatives (**4** and **7a–7g**) were evaluated against ecto-NTPDases, which revealed notable modifications in isoform selectivity and potency (Table 1). Within the series, compound **7g** demonstrated superior inhibitory activity across all isoforms and showed IC_{50} values of 5.13 ± 0.81 μM for NTPDase1, 11.32 ± 0.56 μM for NTPDase2, 1.21 ± 0.23 μM for NTPDase3, and 15.37 ± 1.08 μM for NTPDase8, surpassing the standard suramin. Compound **7d** and **7c** exhibited significant inhibitory activity against NTPDase3. In contrast, compound **7a** and **7e** demonstrated no inhibitory effect on most isoforms, indicating an unfavorable substitution pattern for enzyme binding. Compound **7b** displayed moderate and selective inhibition against NTPDase1 and NTPDase3.

2.2. Structure activity relationship (SAR)

All of the synthesized oxadiazole exhibited moderate to good enzyme inhibitory activity due to the presence of varing pattern of substituents. Particularly compound **7g** showed excellent enzyme inhibitory activity against all NTPDase isoforms compared to other synthesized oxadiaozoles. The presence of acetophenone moiety at heterocyclic sulphur in compound **7g** play very important role in its enzyme inhibitory activity. The high potency of **7g** suggested that the electron withdrawing keto-carbonyl group attached to phenyl ring having no further substituents had profound effect, *via* bonding and nonbonding interactions, on the inhibitory activity. Compound **7d** inhibitory profile also revealed better activity against h-NTPDase3 (IC_{50} 1.98 ± 0.14 μM, strong inhibition), h-NTPDase2 (IC_{50} 17.73 ± 0.88 μM), h-NTPDase8 (IC_{50} 29.58 ± 1.17 μM) and moderate inhibition against h-NTPDase1 (IC_{50} 21.56 ± 1.08 μM). The significantly higher enzyme inhibitory potential of **7d** against three isoforms of NTPDase attributed that presence of

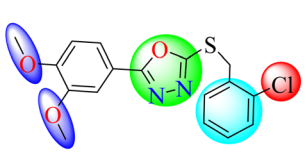

***h*-NTPDase1: 7d** IC_{50} (21.56 ± 1.08 μM)
***h*-NTPDase2: 7d** IC_{50} (17.73 ± 0.88 μM)
***h*-NTPDase3: 7d** IC_{50} (1.98 ± 0.14 μM)
***h*-NTPDase8: 7d** IC_{50} (29.58 ± 1.17 μM)

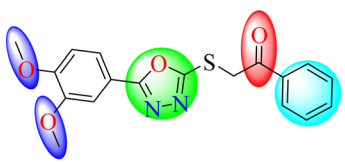

***h*-NTPDase1: 7g** IC_{50} (5.13 ± 0.81 μM)
***h*-NTPDase2: 7g** IC_{50} (11.32 ± 0.56 μM)
***h*-NTPDase3: 7g** IC_{50} (1.21 ± 0.23 μM)
***h*-NTPDase8: 7g** IC_{50} (15.37 ± 1.08 μM)

Fig. 1 Structure activity relationship with highlighted moieties for the best inhibitors **7d** and **7g**.

electronegative halogen –Cl at *ortho* position of phenyl ring is important for its biological activity. The substitution pattern in compound **7g** and **7d** also proved good by the computational molecular docking scores of these oxadiazoles. The Fig. 1 displayed the enzyme inhibitory potential of most potent derivatives **7g** and **7d** with highlighted functional groups involved in inhibition of the target enzyme.

The unsubstituted oxadiazole **4** having no substitution at –SH demonstrated good enzyme inhibitory activity against NTPDase8 and moderate activity against NTPDase1, NTPDase3 while no activity against NTPDase2. It reflects the presence of substituents at –SH particularly acetophenone and halogen substituted phenyl ring increase the enzyme inhibitory potential. The compound **7b** bearing unsubstituted phenyl ring also showed enzyme inhibitory activity against NTPDase1 (IC_{50} 12.26 ± 0.91 μM), NTPDase2 (IC_{50} 23.43 ± 1.36 μM) and NTPDase8 (IC_{50} 36.39 ± 1.52 μM) which is also in good agreement with its docking scores. The derivative **7c** possesses 2-methyl substituted phenyl ring exhibited good activity against NTPDase8 (IC_{50} 31.69 ± 1.37 μM) while moderate enzyme inhibitory activity against all other isoforms of NTPDases. The strongest binding affinity of compound **7c** with docking score (−7.376) against target protein NTPDase8 also proved that presence of electron donating methyl group at ortho position play key role in enzyme inhibition activity. Similarly compound **7f** having 2-methoxy substituted phenyl ring showed good activity aginst NTPDase8 while moderate potential against all other isoforms of NTPDases. It has been observed that presence of electron donating or electronegative substituents at *ortho* position of phenyl ring imparts excellent results in enzyme inhibitory activity. On the other hand presence of electron donating $–OCH_3$ or electronegative halogen –Cl at para position of phenyl ring in compound **7a** and **7e** respectively were not proved good to show NTPDase inhibitory activity.

2.3. Enzyme inhibitory kinetics for 7g

The inhibition kinetics were examined using Lineweaver–Burk plots (Fig. 2) to determine the types of enzyme inhibition exhibited by the most potent derivative, **7g**. The inhibitory kinetics of ecto-NTPDase, as observed with compound **7g**, demonstrated that increasing the substrate concentration resulted in a series of linear plots (straight lines). These lines intersected within the second or third quadrants, either on or away from the *x*-axis. The different concentrations of compounds were incubated with increasing concentration of substrate and the experimental data was subjected to non-linear regression analysis according to Michaelis–Menten equation using the PRISM 5.0 (GraphPad, California, USA). The analysis of NTPDase1 revealed a decrease in the maximal reaction rate (V_{max}) while the Michaelis constant (K_m) remained unchanged at a value of 0.028 μM and with inhibitory constant K_i 0.022 μM. This observation, characterized by an intersection on the *x*-axis in the presence of increasing substrate concentrations, suggests the occurrence of non-competitive inhibition. A similar pattern was observed for NTPDase2, where a group of four straight lines intersected on the *x*-axis in the second quadrant and showed a K_m value of 0.02 μM, indicating noncompetitive inhibition with inhibition constant K_i 0.015 μM. The low K_m values for

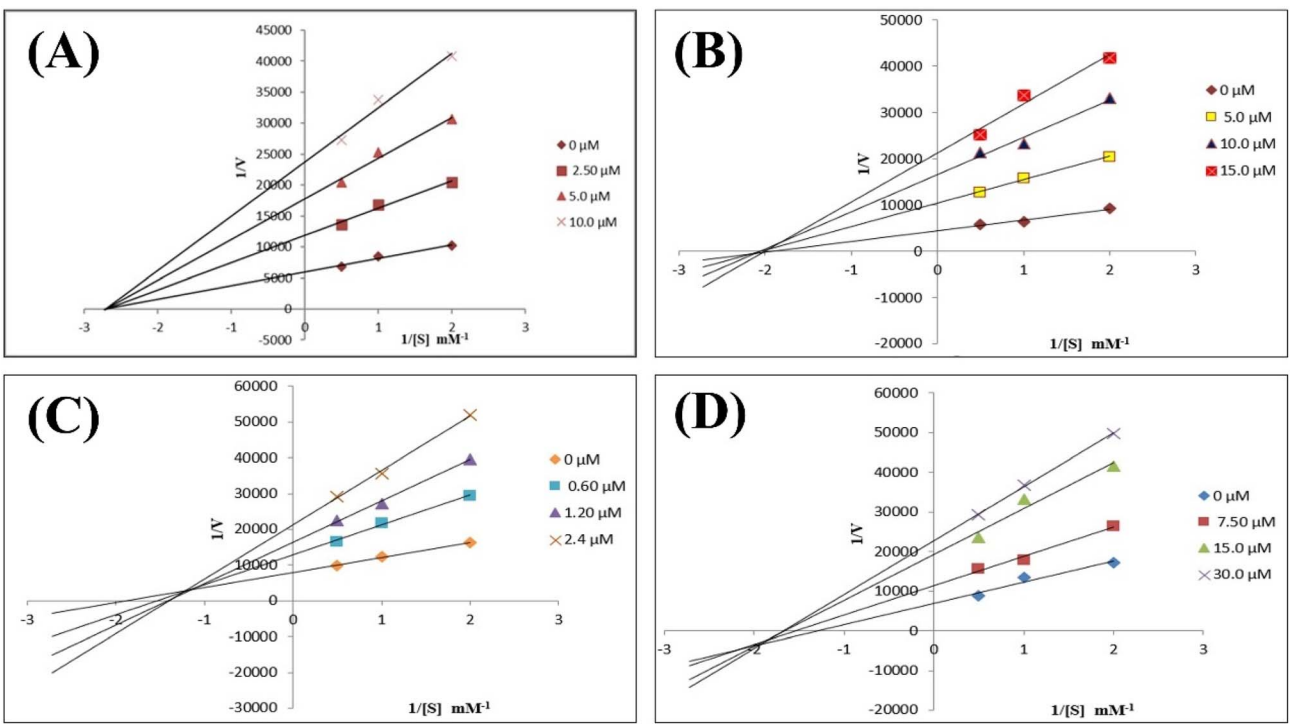

Fig. 2 Lineweaver–Burk plots for the enzyme inhibitory kinetics of **7g** against (A) NTPDase1, (B) NTPDase2, (C) NTPDase3, and (D) NTPDase8. The **7g** concentrations used against NTPDase1 (0, 2.5, 5.0, 10.0 μM), against NTPDase2 (0, 5.0, 10.0, 15.0 μM), against NTPDase3 (0, 0.6, 1.2, 2.4 μM), against NTPDase1 (0, 7.5, 15.0, 30.0 μM). The different concentrations of substrate used were 0.5, 1.0 and 2.0 mM.

Table 2 DFT calculation (quantum chemical descriptors) of the selected ligands and redocked standards in aqueous phase

Ligands	Dipole moment (debye)	HOMO (a.u.)	LUMO (a.u.)	Energy gap (ΔE_{Gap})	Ionization potential (eV)	Electron affinity (eV)	Electro-negativity χ (eV)	Electro-chemical potential μ (eV)	Hardness η (eV)	Softness S (eV^{-1})	Electrophilicity ω (eV)
7g	12.363962	−0.2045	−0.0714	0.1331	5.5647	1.9429	3.7538	−3.7538	1.8109	0.5522	3.8906
4	8.5380660	−0.2067	−0.0571	0.1496	5.6246	1.5538	3.5892	−3.5892	2.0354	0.4913	3.1645
7d	8.0666460	−0.2051	−0.0554	0.1497	5.5811	1.5075	3.5443	−3.5443	2.0368	0.4910	3.0838
7c	9.1357910	−0.2030	−0.0529	0.1502	5.5271	1.4393	3.4832	−3.4832	2.0440	0.4892	2.9693
Amp	11.974072	−0.2214	−0.0344	0.1870	6.0246	0.9361	3.4803	−3.4803	2.5437	0.3931	2.3807
Anp	16.754140	−0.2214	−0.0421	0.1793	6.0246	1.1456	3.5851	−3.5851	2.4389	0.4101	2.6324

both NTPDase1 and 2 indicate strong binding affinities between the enzyme and inhibitor complexes. For NTPDase3, the maximal reaction rate (V_{max}) was found to decrease with varying values of K_m in the presence of increasing concentrations of substrate due to the intersection of lines away from the *x*-axis but still within the second quadrant, and it exhibited a mixed-type of inhibition with inhibition constant K_i 1.13 μM. The increase in K_m values for mixed-type inhibition of NTPDase3 indicated that inhibitor **7g** preferred to bind to the enzyme (E) rather than the enzyme–substrate (ES) complex. On the contrary, V_{max} again decreased in the case of NTPDase8, but with a decrease in K_m values due to intersections of the lines in the third quadrant showing a mixed-type mode of inhibition with inhibition constant 12.4 μM against NTPDase8 was revealed, which proved that **7g** preferred to bind the enzyme–substrate (ES) complex (Fig. 2).

2.4. MEP and chemical reactivity of 1,3,4-oxadiazoles as ecto-NTPDases inhibitors

Table 2 and Fig. 3 present the DFT computations for the leading hit and most effective inhibiting oxadiazoles, alongside the

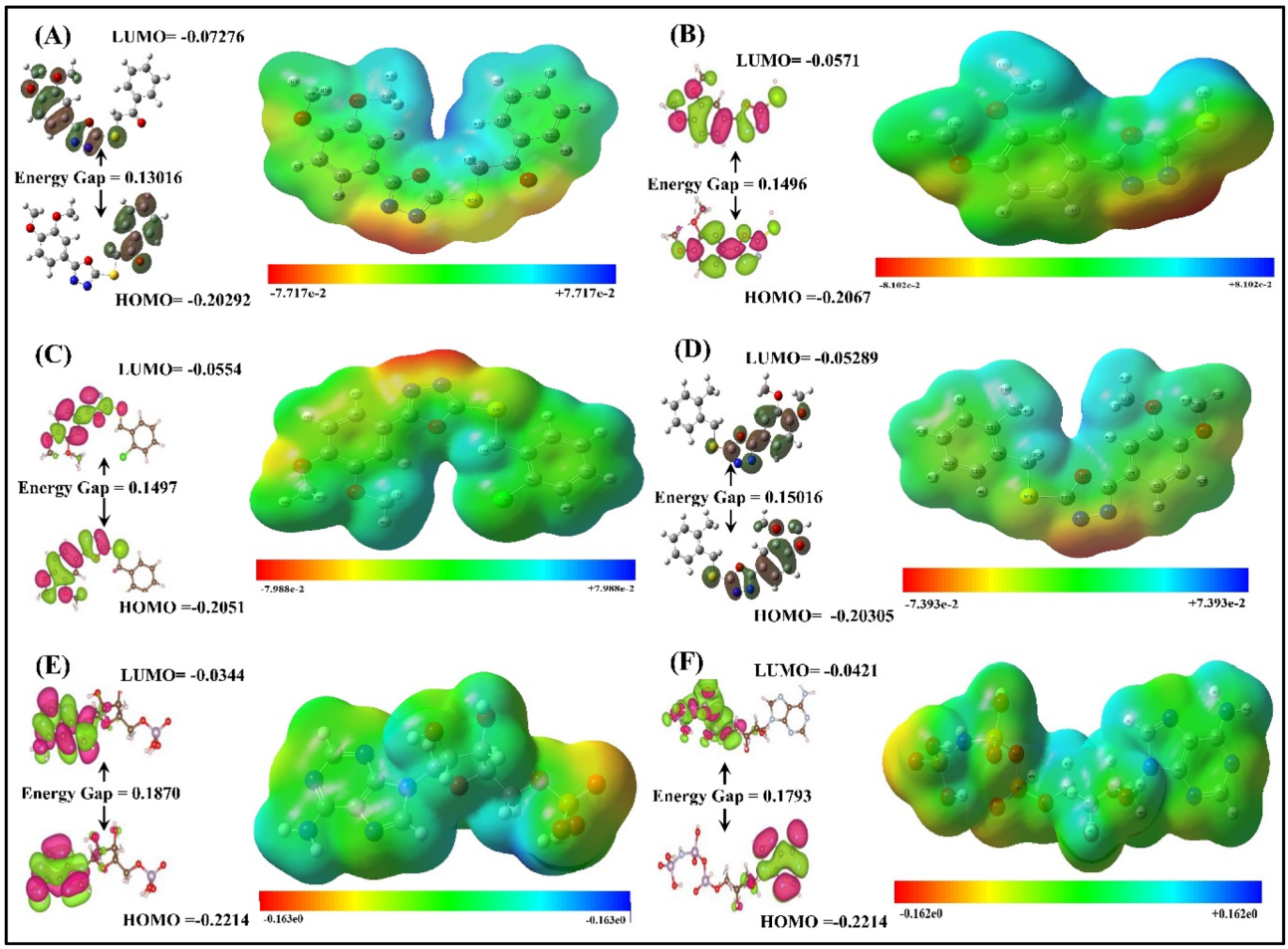

Fig. 3 MEP for leading hits ligands & inhibitors; (A) **7g** for NTPDase1, (B) **4** (thiol) for NTPDase2, (C) **7d** for NTPDase3, (D) **7c** for NTPDase8, (E) **Amp** as redocked standard, (F) **Anp** as redocked standard.

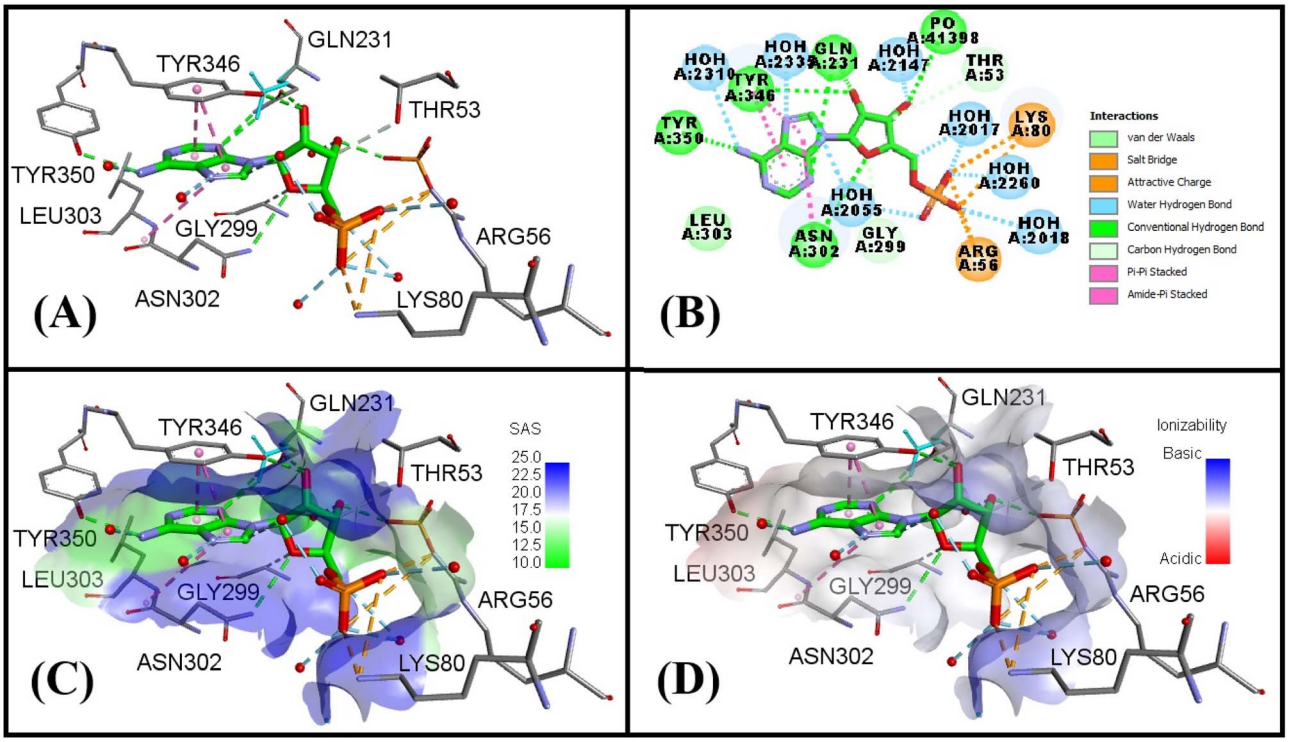

Fig. 4 Binding pocket analysis for NTPDase1 (4BRQ) containing co-crystallized ligand **Amp1396** (green); (A) 3D diagram for ligand's interactions, (B) 2D diagram for ligand's interactions, (C) solvent accessibility surface, (D) ionizability surface.

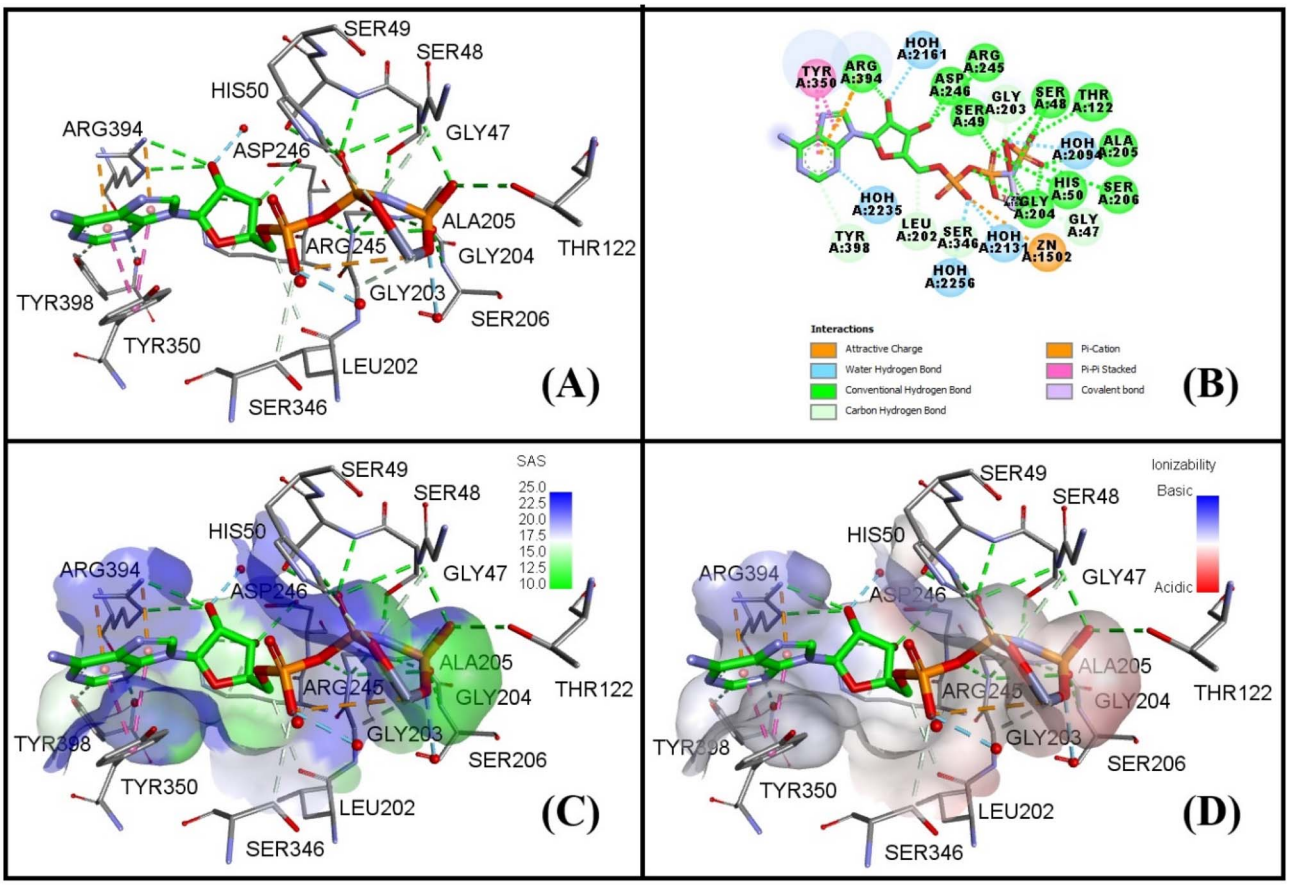

Fig. 5 Binding pocket analysis for NTPDase2 (4BR5) containing co-crystallized ligand, **Anp1501** (green); (A) 3D diagram for ligand's interactions (B) 2D diagram for ligand's interactions, (C) solvent accessibility surface, (D) ionizability surface.

redocked standards **Amp** and **Anp**, for NTPDases1, 2, 3, and 8. These computations utilize key quantum chemical descriptors to assess stability, reactivity, and interaction potential of **4** and **7a–7g**. Fig. 3 shows the molecular electrostatic potential (MEP) surface and frontier molecular orbitals (FMO) of compounds **7g**, **4**, **7d**, **7c**, **Amp**, and **Anp**. In the MEP surface graphs, green sections of graph showed neutral regions, responsible for hydrophobic interactions such as π–π stacking. The blue sections show electron-deficient parts of the compounds and regions of the hydrogen bond donor. In contrast, the red sections act as hydrogen bond acceptors and are electron-rich regions of compounds that are favorable to electrophiles. Green, blue (hydrogen bond donor), and red (hydrogen bond acceptor) are more prominent on the MEP of 1,3,4-oxadiazoles in Fig. 3(A)–(D) as compared to the redocked standards **Amp** and **Anp**, as shown in (E) and (F).

Moreover, the HOMO and LUMO orbitals in Fig. 3 indicated that electron distributions were not equal over the entire molecular structure. This observation indicated a particular molecular architecture which was dominant while determining the electronic properties of molecule. The HOMO and LUMO of compound **4** were present over the whole molecule and showed dominant interactions of the whole molecule with NTPDase2. Similarly, the HOMOs and LUMOs of compounds **7g** and **Anp** had a complementary distribution as they were not distributed on the same parts of the molecules. This indicated that the whole molecule of **7g** and **Anp** were involved in interactions or reactivity towards the corresponding ecto-NTPDases. On contrary, molecules (C) to (E) present in Fig. 3 had their HOMO and LUMO orbitals localized on the same but small parts of the molecules and showed reduced interactions. These findings demonstrated that 1,3,4-oxadiazoles, particularly (**7g**), represented a balanced MEP surface along with good docking scores and supported the best inhibitory activity.

Quantum chemical descriptors given in Table 2 reflected the chemical reactivity and interactions of 1,3,4-oxadiazoles with top docking scores and IC_{50} values. The dipole moments varied from 8.0666460 debye for **7d** to 16.754140 debye for **Anp**, while HOMO energies ranged between −0.2214 a.u. for both **Amp** and **Anp** and −0.2067 a.u. for **4**. LUMO energies spanned from −0.0714 a.u. for **7g** to −0.0344 a.u. for **Amp**. The calculated energy gap (ΔE_{Gap}) extended from 0.1331 for **7g** to 0.1870 for **Amp**, whereas the ionization potential ranged from 5.5271 eV for **7c** to 6.0246 eV for both **Amp** and **Anp**. Electron affinity varied from 0.9361 eV for **Amp** to 1.9429 eV for **7g**. Electronegativity (χ) values were observed between 3.4803 eV for **Amp** and 3.7538 eV for **7g**, with corresponding electrochemical potential (μ) values ranging from −3.7538 eV for **7g** to −3.4803 eV for **Amp**. Chemical hardness (η) varied from 1.8109 eV for **7g** to 2.5437 eV for **Amp**, while softness (S) ranged between 0.3931 eV^{-1} for **Amp** and 0.5522 eV^{-1} for **7g**. Finally, electrophilicity index (ω) values were distributed from 2.3807 eV for **Amp** to 3.8906 eV for **7g**, indicating notable variability across the studied compounds, with **7g** and **Amp** frequently showing extreme values for these quantum chemical descriptors.

The dipole moment of ligand **7g** was 12.364 debye, indicating moderately high polarity in the aqueous phase. The HOMO and LUMO energies were −0.2045 a.u. and −0.0714 a.u., respectively, while the energy gap (ΔE_{Gap}) was 0.1331 a.u. (3.618 eV), which suggested balanced chemical reactivity. The calculated ionization potential was 5.5647 eV, and the electron affinity was 1.9429 eV, reflecting its moderate ability to donate or accept electrons. Its electronegativity and electrochemical potential were 3.7538 eV and −3.7538 eV, respectively,

Table 3 Residue ligand interactions of ligand **7g**, **4**, **7d**, and **7c** with ecto-NTPDases

Sr. no.	Residue – ligand	Distance (Å)	Interaction type
NTPDase1 & 7g			
1	HOH2055 – 7g	2.91868	Hydrogen bond
2	7g – SER235	2.99203	Hydrogen bond
3	7g – GLN349	3.44973	Hydrogen bond
4	THR53 – 7g	3.27031	Hydrogen bond
5	THR232 – 7g	3.64544	Hydrogen bond
6	TYR346 – 7g	2.65860	Hydrogen bond
7	TYR346 – 7g	3.69724	Pi–Pi stacked
8	7g – TYR346	5.06308	Pi–Pi T-shaped
NTPDase2 & 4 (thiol)			
1	Zn1502 – 4	2.62200	Electrostatic
2	HOH2056 – 4	2.69029	Hydrogen bond
3	HOH2094 – 4	2.84318	Hydrogen bond
4	HOH2131 – 4	3.05125	Hydrogen bond
5	SER49 – 4	2.13892	Hydrogen bond
6	HIS50 – 4	2.11405	Hydrogen bond
7	THR122 – 4	3.07354	Hydrogen bond
8	GLY203 – 4	2.46681	Hydrogen bond
9	4 – ASP246	2.54703	Hydrogen bond
10	4 – ASP246	2.51100	Hydrogen bond
11	4 – ARG245	3.69690	Hydrophobic
12	TYR350 – 4	4.93951	Pi-alkyl
NTPDase3 & 7d			
1	ARG388 – 7d	2.84633	Hydrogen bond
2	ARG388 – 7d	1.91361	Hydrogen bond
3	ARG388 – 7d	2.60781	Hydrogen bond
4	7d – ASP556	2.30305	Hydrogen bond
5	7d – MET329	2.45686	Hydrogen bond
6	MET329:ALA330 – 7d	4.45647	Amide-Pi stacked
7	GLY492:GLY493 – 7d	3.87631	Amide-Pi stacked
8	ALA333 – 7d	3.90069	Alkyl
9	7d – ARG388	5.06831	Alkyl
10	MET329 – 7d	4.82380	Pi-alkyl
11	7d – ALA330	4.12798	Pi-alkyl
12	7d – ALA496	4.29041	Pi-alkyl
13	7d – LEU553	3.93168	Pi-alkyl
NTPDase8 & 7c			
1	SER51 – 7c	2.29803	Hydrogen bond
2	SER52 – 7c	1.90854	Hydrogen bond
3	7c – ASP48	2.18898	Hydrogen bond
4	SER52 – 7c	2.49202	Hydrogen bond
5	ASN354 – 7c	2.31831	Hydrogen bond
6	TYR357 – 7c	5.12174	Pi–Pi stacked
7	TRP398 – 7c	4.10926	Pi–Pi stacked
8	ALA126 – 7c	4.48440	Alkyl
9	ALA209 – 7c	4.48505	Alkyl
10	TYR357 – 7c	4.64604	Pi-alkyl
11	TRP398 – 7c	5.28275	Pi-alkyl
12	TRP440 – 7c	4.84206	Pi-alkyl

indicating that it had a fair tendency to attract electrons. Lowest hardness (η) of 1.8109 eV and highest softness (S) of 0.5522 eV^{-1} indicated that the molecule will preferably show interact with the softer moieties of enzyme. Finally, the electrophilicity index of 3.8906 eV suggested that **7g** could act as a very good electrophile in interactions with nucleophilic targets owing to the presence of a keto-carbonyl group.

The **Amp** ligand exhibited a higher dipole moment of 11.974 debye, reflecting its significant polarity in the aqueous phase. Furthermore, the HOMO and LUMO energies were −0.2214 and −0.0344 a.u., respectively, with an energy gap of 0.1870 a.u. (≈5.09 eV), reflecting a relatively stable and less reactive molecule. An ionization potential of 6.0246 eV and an electron affinity of 0.9361 eV indicated that **Amp** was more reluctant to donate or accept electrons than the other ligands. Its electronegativity was 3.4803 eV, and the electrochemical potential was −3.4803 eV, indicating a moderate electron-attracting ability. From the obtained values of hardness, 2.5437 eV, and softness, 0.3931 eV^{-1}, it is obvious that **Amp** was found to be relatively hard and less reactive. Its electrophilicity was 2.3807 eV, indicating moderate potential toward electrophilic interactions.

2.5. Homology modelling and docking studies

Ligand **Amp1396** (green) was found to be embedded in the cavity of chain A of NTPDase1 (PDB ID: 4BRQ), and amino acid residues (Tyr350, Asn302, Lys80, and Tyr346) were present at the entrance channel of active site, as shown in Fig. 4.

The 3D and 2D diagrams in Fig. 4, panels (A) and (B), revealed important interactions of ligand **Amp1396** with the amino acid residues located on active site of NTPDase1 enzyme. The solvent accessibility surface, panel (C), presents a solvent-accessible surface (SAS) analysis of ligand **Amp1396** (green) within the binding pocket. A color gradient ranging from green to blue indicated various levels of solvent accessibility, with green being the least accessible region and blue indicating the area more exposed to solvent. Fig. 4 panel (D) illustrates the ionization surface of NTPDase1's binding pocket, showing how electrostatic features influence ligand binding (Fig. 4). Red and blue gradients marked the acidic to basic regions responsible for hydrogen bonding and electrostatic interactions around the original ligand **Amp1396**.

Co-crystallized ligand **Anp1501** (green) was located within the cavity of chain A of NTPDase2 (PDB ID: 4BR5), with amino acid residues Tyr350, Arg394, His50, and Ser346 positioned at the entrance of the active site channel. The multiple interactions of ligand **Anp1501** (green) within the binding pocket of NTPDase2 were responsible for its stability and affinity toward the enzyme, further reinforcing its position. These affinities suggested that polarity in the binding pocket contributed to ligand stabilization, which was confirmed by the solvent accessibility and ionizability surfaces in Fig. 5. The ligand **Amp700** (green) was co-crystallized within the cavity of chain A of NTPDase3 (PDB ID: 4A59), as illustrated in Fig. S1 (SI), with amino acid residues Ala496 and Leu553 located at the entrance of the active site channel. The interactions between the ligand **Amp700** and amino acids of NTPDase3 showed a variety of binding interactions which contributed to the straining of the ligand at the active site, as shown in panels (A) and (B) of Fig. S1 (SI). The solvent accessibility surface (SAS) in panel (C) around ligand **Amp700** in the binding pocket of NTPDase3 seemed to be partially embedded within the active site, with most regions (blue) exposed to the solvent, while others were shielded by nearby amino acids. The ionizability surface around **Amp700** in panel (D) of Fig. S1 (SI), displayed a neutral gray representation, indicating that there were no distinct acidic or basic regions in the binding pocket of NTPDase3.

The docking validations for NTPDase1–3, depicted in panel (B) of the Fig. S2–S4 (SI), revealed RMSD values of 0.3040 Å, 0.6844 Å, and 0.4943 Å, respectively, between the co-crystallized (green) and redocked ligands (cyan). An RMSD value below 2.0 Å is generally regarded as a strong indicator of reliable docking performance. Low RMSD values confirmed that the docking protocols for NTPDase1–3 effectively reproduced the experimentally determined binding conformations with high accuracy for further computational and structural analysis. NTPDase8 was constructed acquiring the sequence of amino acids from UNIPROT database and modelling with SWISS homology modelling server and choosing the homology model based on NTPDase2 (PDB ID: 3CJ9) with a sequence identity of 46.19% and global model quality estimate (GMQE) score of 0.69, indicating a good quality homology model with minor deviations, as indicated by the visual comparison between PDB

Table 4 Docking scores of the selected ligands against the ecto-NTPDases

	Docking scores			
Ligands	NTPDase1	NTPDase2	NTPDase3	NTPDase8
4-thiol	−3.925	−6.079	−2.971	−4.202
4-thione	−1.658	−1.955	−2.300	−1.080
7a	−3.590	−3.740	−2.880	−5.519
7b	−4.821	−3.465	−3.269	−6.174
7c	−4.010	−4.133	−2.983	−7.376
7d	−4.681	−3.952	−3.452	−6.552
7e	−4.123	−3.619	−2.124	−6.255
7f	−4.167	−2.946	−3.070	−6.701
7g	−5.171	−4.742	−3.360	−4.660
Redocked standards	**Amp**	**Anp**	**Amp**	**No redocked standard used**
	−13.410	−12.881	−8.176	

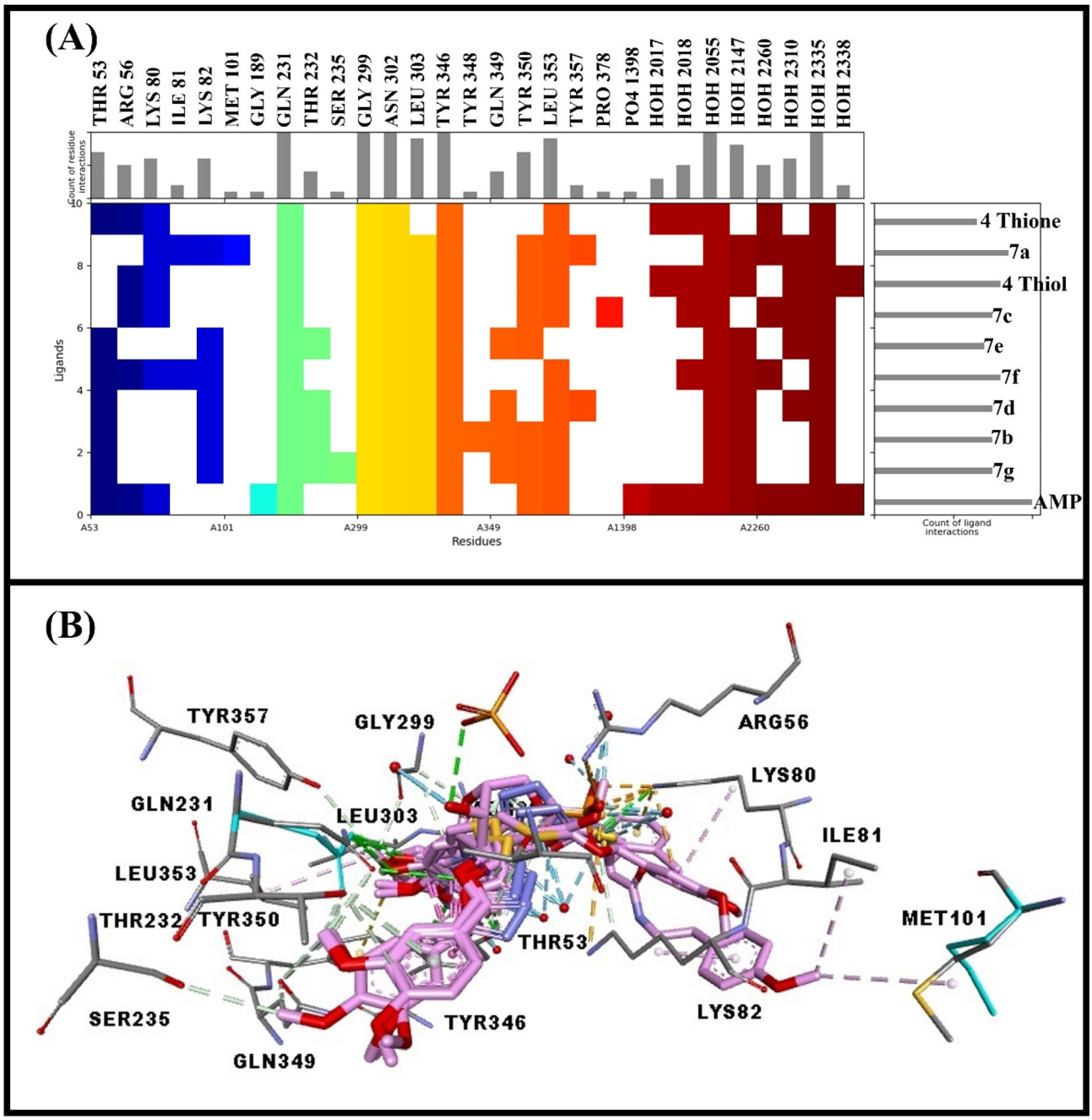

Fig. 6 SIFt Analysis for NTPDase1; (A) heat map depicting interactions of ligands with different amino acid residues and water molecules, (B) 3D diagram showing all docked ligands.

3CJ9 in the panel (A) and homology model (B), as well as the *Z* score in the panel (C) of figure lying between −2 and −1 proved that it to be a reliable homology model. The molprobity results for Ramachandran plot in Fig. S5 (SI), (D) and (E) indicating the stereochemical quality of NTPDase8 homology model were evaluated and the results indicated an overall good-quality structure. The MolProbity score of 1.65 reflected a well-refined model that was comparable to high-resolution experimentally determined protein structures. This low score suggested that the global geometry and packing of homology model were reliable and within acceptable limits for structural analysis.

The clash score of 5.61 indicated a small number of steric overlaps, primarily involving residue pairs such as Leu260–His271, Phe359–Phe429, Cys316–Leu407, and Arg264–Glu322. These clashes were relatively minor and localized, suggesting that they did not significantly compromise the overall fold of homology model. Instead, they likely arose from side-chain conformations that could be further optimized without altering the backbone architecture. Analysis of backbone dihedral angles showed that 95.01% of residues were located in favored regions of the Ramachandran plot, demonstrating good conformational agreement with known protein *i.e.* 3CJ9. Only

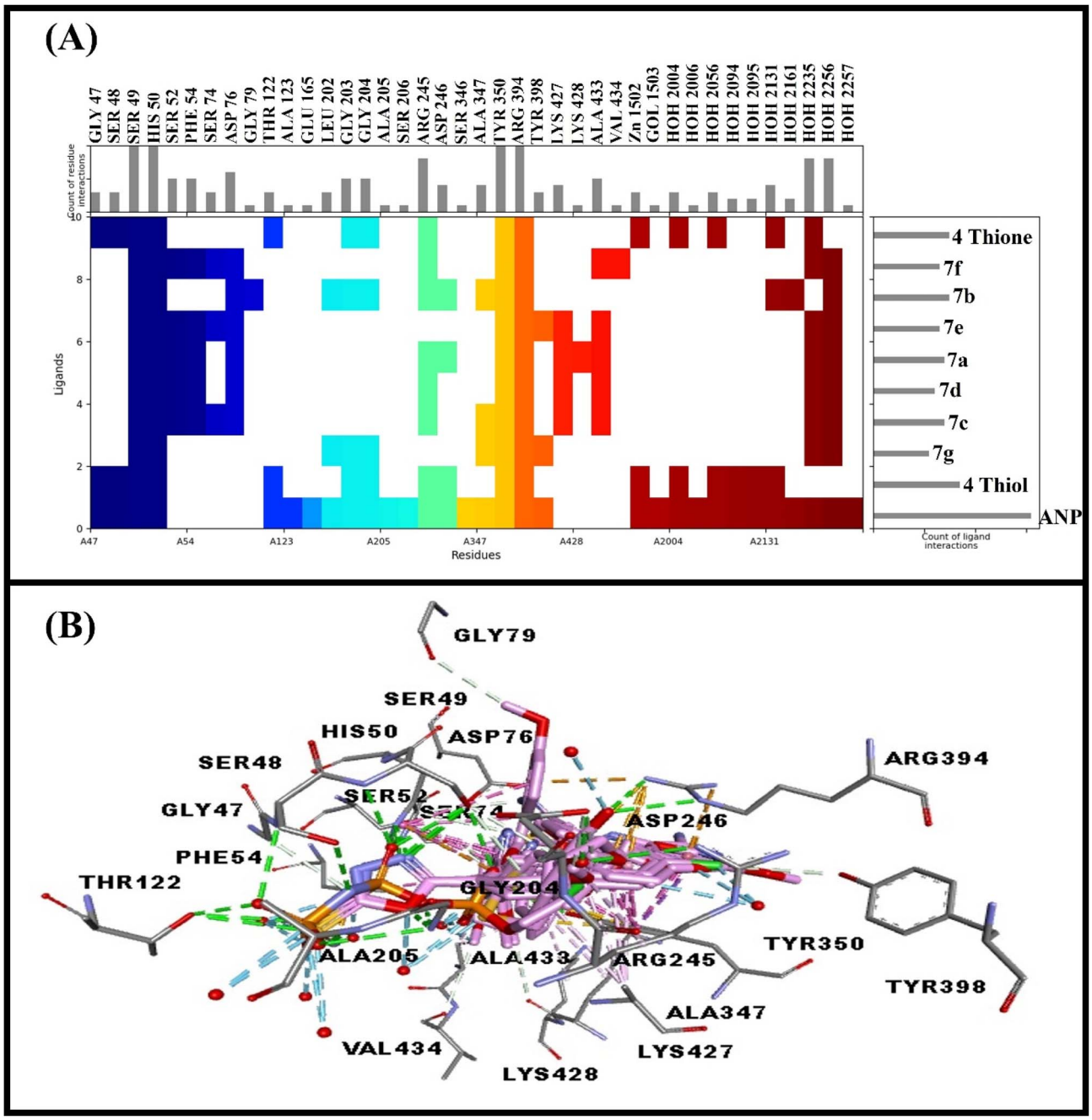

Fig. 7 SIFt analysis for NTPDase2; (A) heat map depicting interactions of ligands with different amino acid residues and water molecules, (B) 3D diagram showing all docked ligands.

0.95% of residues were classified as outliers, including Arg270, Pro217, Ser187, and Pro297. The low proportion of outliers supported the structural integrity of the model, although these specific residues may correspond to flexible or poorly constrained regions that warrant cautious interpretation.

Side-chain geometry was also well maintained, with only 0.29% rotamer outliers, limited to a single residue (Leu260). Additionally, only one Cβ deviation was observed (Trp192), indicating minimal distortion in local backbone geometry. The absence of bad bonds further confirmed that bond lengths were within acceptable parameters, while only 18 out of 4597 bond angles were flagged as unfavourable, representing a negligible fraction. These validation metrics suggested that the NTPDase8 homology model was structurally reliable and suitable for downstream analyses such as molecular docking or functional interpretation. Among the ligands evaluated for NTPDase1, as detailed in Table 4, compound **7g** demonstrated the most favorable docking score of −5.171 and indicated a strong binding affinity, as illustrated in Fig. S6 (SI). Interactions between the residues and ligand, including distances and interaction types, are also presented in Table 3. Compounds **7b** (−4.821), **7d** (−4.681), and **7c** (−4.010) also showed appreciable

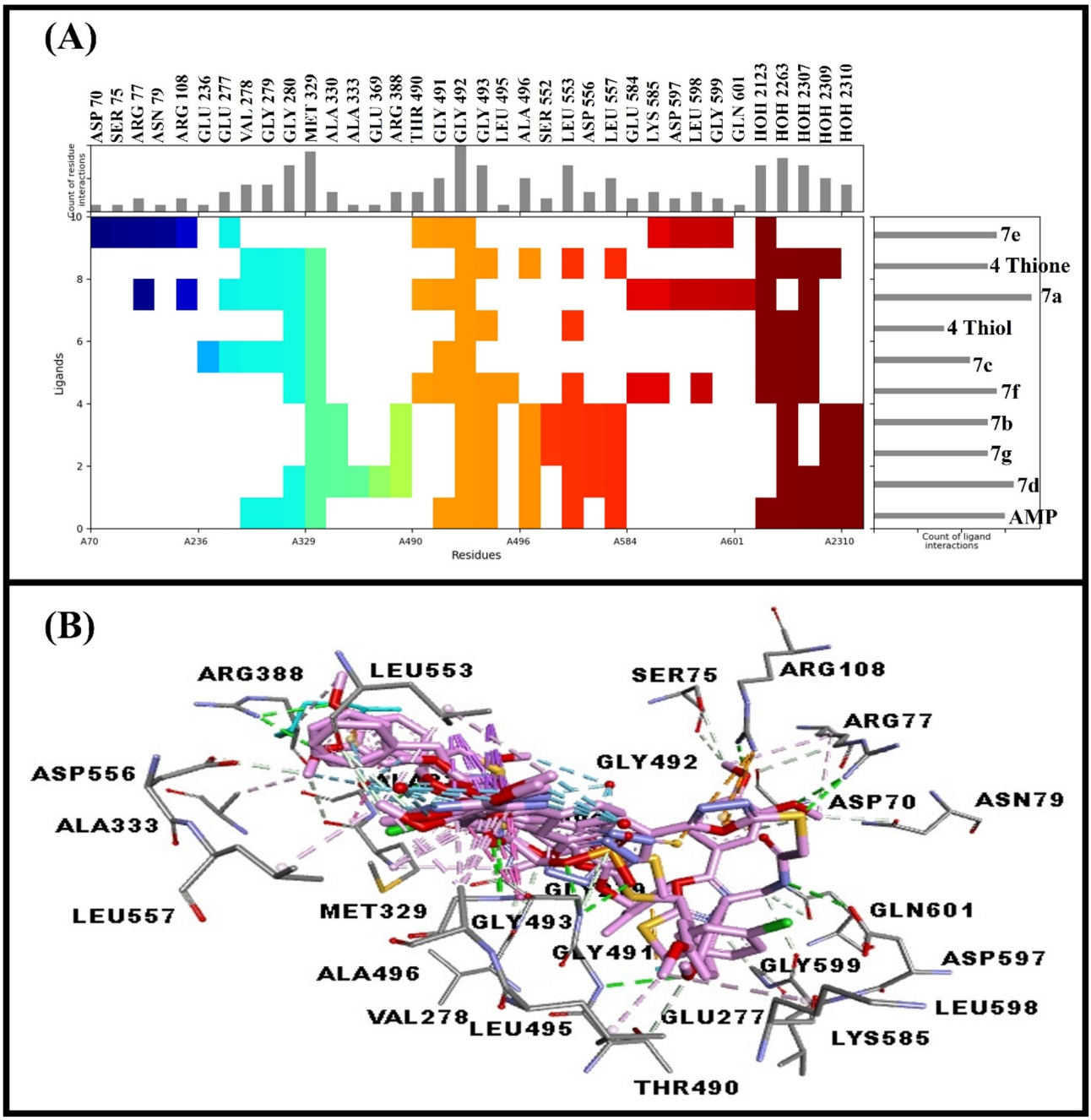

Fig. 8 SIFt analysis for NTPDase3; (A) heat map depicting interactions of ligands with different amino acid residues and water molecules, (B) 3D diagram showing all docked ligands.

interactions, while the **4**-thiol derivative (−3.925) displayed moderate affinity.

In case of NTPDase2, as given in Table 4, the **4**-thiol derivative showed a relatively strong docking score of −6.079, depicted in Fig. S7 (SI) and its residue–ligand interactions, distances, and interaction types were mentioned in Table 3. Compound **7g** also demonstrated a notable binding score of −4.742, followed by **7c** (−4.133), and **7d** (−3.952).

For NTPDase3, the most favorable docking score was observed for **7d** (−3.452), as shown in Fig. S8 (SI), along with residue–ligand interactions, distances, and interaction types given in Table 3, followed closely by **7g** (−3.360) and **7b** (−3.269). Docking results for NTPDase8, given in Table 4, showed that compound **7c** displayed the strongest affinity at −7.376, as shown in Fig. S9 (SI), along with its interactive description given in Table 3, followed by **7f** (−6.701) and **7d** (−6.552).

2.6. Mechanistic insights through structural interaction fingerprint (SIFt) analysis

For deeper insight into the docking results, structural interaction fingerprint (SIFt) analysis was carried out for each of the

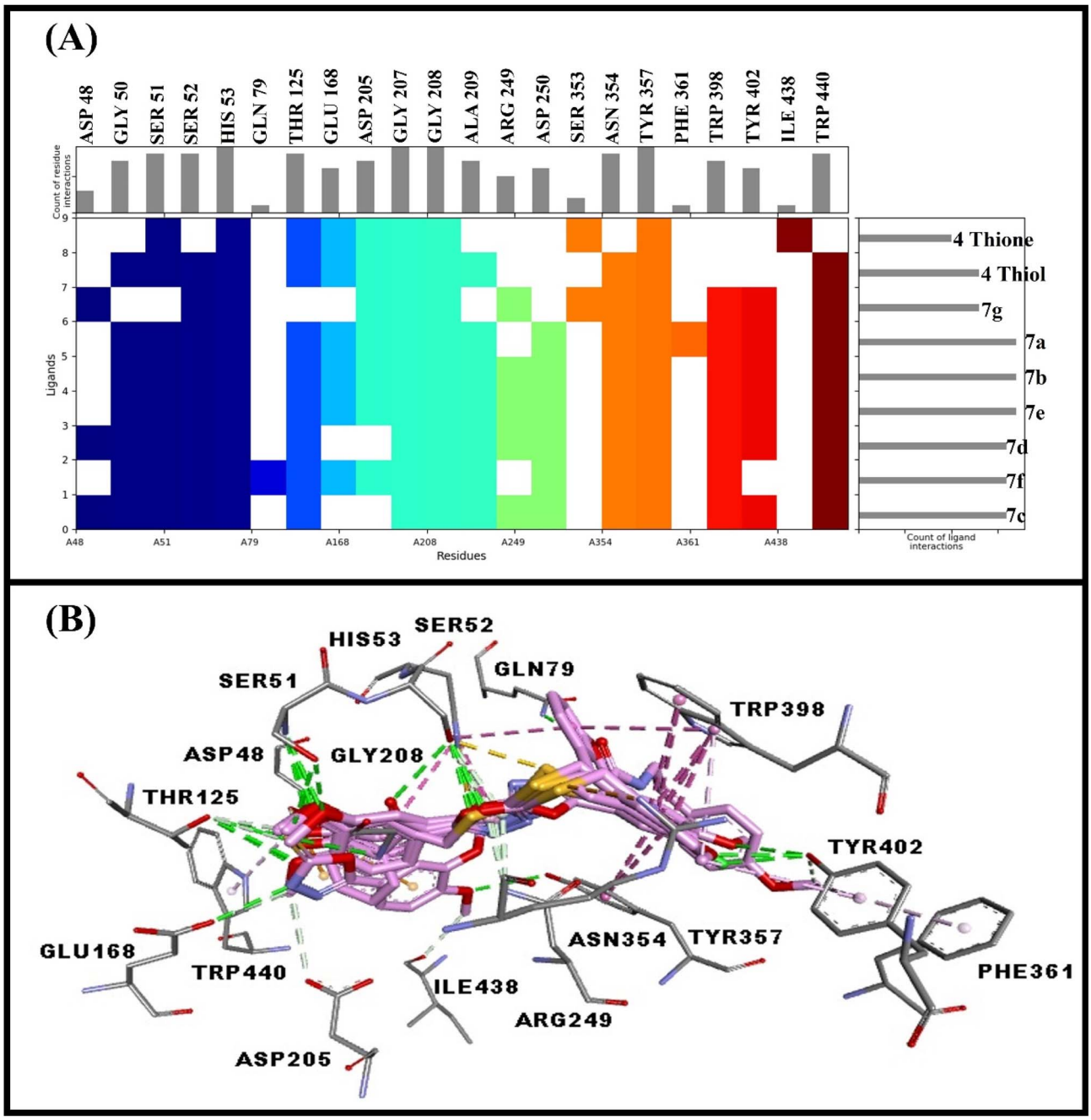

Fig. 9 SIFt analysis for NTPDase8; (A) heat map depicting interactions of 1,3,4-oxadiazoles with different amino acid residues (B) 3D diagram showing all docked ligands.

ecto-NTPDase enzymes using Maestro 12.5 Schrödinger. The Structural Interaction Fingerprint (SIFt) plot in Fig. 6 illustrates the patterns of NTPDase1 (4BRQ) protein interactions with a set of synthesized 1,3,4-oxadiazole derivatives named **4** (thiol and thione), **7a–7g**, and the redocked reference ligand **Amp**. The rows in heat map represent the oxadiazole derivative, whereas the columns represent a single amino acid residue of NTPDase1.

Analysis revealed that certain residues, such as Gln231, Gly299, Asn302, and Tyr346, presented the highest interaction frequencies among all available ligands. Notably, the redocked standard **Amp** (at the bottom of the heatmap) shared interaction profiles with all the water molecules more than the proximate ligands *i.e.* **7g** and **7b**, indicating that **Amp** had a better docking score owing to most of the water molecule-based interactions.

SIFt plot in Fig. 7 described the interaction profile between NTPDase2 and a collection of 1,3,4-oxadiazoles, that is, **4** (thiol and thione), **7a–7g**, and the redocked reference ligand **Anp**. The heat map for NTPDase2 shows that certain residues, such as Ser49, His50, Tyr350, and Arg394, are always present in ligand interactions and form the core region of binding site. Among

Table 5 pkCSM pharmacokinetic parameters of the synthesized compounds (**4**, **7a–7g**)

Pharmacokinetic properties		Selected compounds							
Properties	Model name	**4**	**7a**	**7b**	**7c**	**7d**	**7e**	**7f**	**7g**
Absorption	Water solubility	−2.886	−5.126	−4.819	−5.081	−5.282	−5.216	−4.823	−4.91
	Caco2 permeability	1.282	0.97	1.433	1.429	1.079	1.09	1.24	1.256
	Intestinal absorption (human)	94.095	91.772	95.49	95.198	93.739	94.108	96.233	95.681
	Skin permeability	−2.81	−2.777	−2.663	−2.659	−2.674	−2.683	−2.718	−2.681
	P-glycoprotein substrate	No	Yes	No	No	No	No	No	No
	P-glycoprotein I inhibitor	No	Yes	Yes	Yes	Yes	Yes	Yes	Yes
	P-glycoprotein II inhibitor	No	Yes	Yes	Yes	Yes	Yes	Yes	Yes
Distribution	VDss (human)	−0.158	−0.189	−0.127	−0.043	−0.068	−0.082	−0.091	−0.28
	Fraction unbound (human)	0.306	0	0.069	0.062	0.052	0.084	0.077	0.039
	BBB permeability	0.261	−0.974	0.228	0.21	0.197	0.201	−0.214	−0.958
	CNS permeability	−2.947	−3.217	−2.235	−2.163	−2.122	−2.117	−2.414	−2.466
Metabolism	CYP2D6 substrate	No	No	No	No	No	No	No	No
	CYP3A4 substrate	No	Yes	Yes	Yes	Yes	Yes	Yes	Yes
	CYP1A2 inhibitor	Yes	No	Yes	Yes	Yes	Yes	Yes	Yes
	CYP2C19 inhibitor	No	Yes	Yes	Yes	Yes	Yes	Yes	Yes
	CYP2C9 inhibitor	No	Yes	Yes	Yes	Yes	Yes	Yes	Yes
	CYP2D6 inhibitor	No	No	No	No	No	No	No	No
	CYP3A4 inhibitor	No	Yes	No	Yes	Yes	Yes	Yes	No
Excretion	Total clearance	0.389	0.419	0.373	0.273	0.304	0.24	0.409	0.553
	Renal OCT2 substrate	No	No	No	No	No	No	No	No
Toxicity	AMES toxicity	No	No	No	No	No	No	No	No
	Max. tolerated dose (human)	0.992	0.614	0.797	0.791	0.797	0.743	0.815	0.974
	hERG I inhibitor	No	No	No	No	No	No	No	No
	hERG II inhibitor	No	Yes	Yes	Yes	Yes	Yes	Yes	Yes
	Oral rat acute toxicity (LD_{50})	2.188	2.449	2.037	2.147	2.244	2.199	2.273	2.111
	Oral rat chronic toxicity (LOAEL)	0.978	0.912	1.217	1.263	1.036	1.031	1.14	1.198
	Hepatotoxicity	Yes	Yes	Yes	Yes	No	No	Yes	Yes
	Skin sensitisation	No	No	No	No	No	No	No	No
	T. pyriformis toxicity	0.685	0.36	0.475	0.493	0.474	0.461	0.401	0.457
	Minnow toxicity	1.365	0.095	−1.516	−1.651	−1.869	−1.736	−1.529	−1.453

the 1,3,4-oxadiazoles, **4** (thiol and thione) and **7g** interacted actively and strongly with these residues, indicating a stable binding orientation (Fig. 7). The redocked reference **Anp** displayed an unambiguous interaction pattern, binding tightly to core residues as well as to all of water molecules present in the vicinity that assisted **Anp** in obtaining an improved docking score over oxadiazoles **4** and **7g** (Fig. 7).

SIFt plot in Fig. 8 describes the patterns of interaction of NTPDase3 (4A59) protein with a series of synthesized oxadiazole derivatives **4** (thiol and thione), **7a–7g**, and the redocked reference ligand **Amp**. Analysis indicated that some residues, such as Met329, Gly492, and HOH2263, showed the highest frequencies of interaction among all available ligands. The redocked control **Amp** (at the bottom of the heatmap) had interaction profiles with all the water molecule which explains why **Amp** possessed an improved docking score due to the majority of water molecule-based interactions.

SIFt plot in Fig. 9 accounted for patterns of interactions of target enzyme NTPDase8 obtained through homology modelling (therefore without redocked standard and water molecules near the binding pocket) with a series of synthesized 1,3,4-oxadiazole derivatives **4** (thiol and thione) and **7a–7g**. Analysis revealed that some residues, such as His53, Gly207, Gly208, and Tyr357, exhibited the highest frequencies of interaction with all accessible ligands. Water-mediated interactions were not present for this homology-modelled protein.

2.7. *In silico* pharmacokinetic evaluation through pkCSM and SwissADME

The pharmacokinetic analysis of pkCSM, as shown in Table 5, provided critical insights into the absorption, distribution, metabolism, excretion, and toxicity (ADME/T) properties of the selected compounds (**4**, **7a–7g**), offering a comprehensive understanding of their pharmacokinetic profiles.

Compounds **7d** and **7e** exhibited outstanding safety and pharmacokinetic profiles, characterized by non-hepatotoxicity, minimal toxicity to minnows, and favorable absorption and metabolic properties. Compound **4** was also notable for its solubility, lack of interactions with *P*-glycoprotein, and absence of CYP inhibition, rendering it a strong candidate for further investigation. These findings collectively underscore the significance of balancing ADME/T parameters to identify potential drug candidates with optimal efficacy and safety profiles. Compounds **4**, **7d**, and **7g** were particularly distinguished by superior probability values across multiple parameters, resulting in a relatively balanced and safe toxicological profile. The heat map in Fig. S10 (SI) illustrated compounds **4** and **7a–7g** possessed several commendable properties.

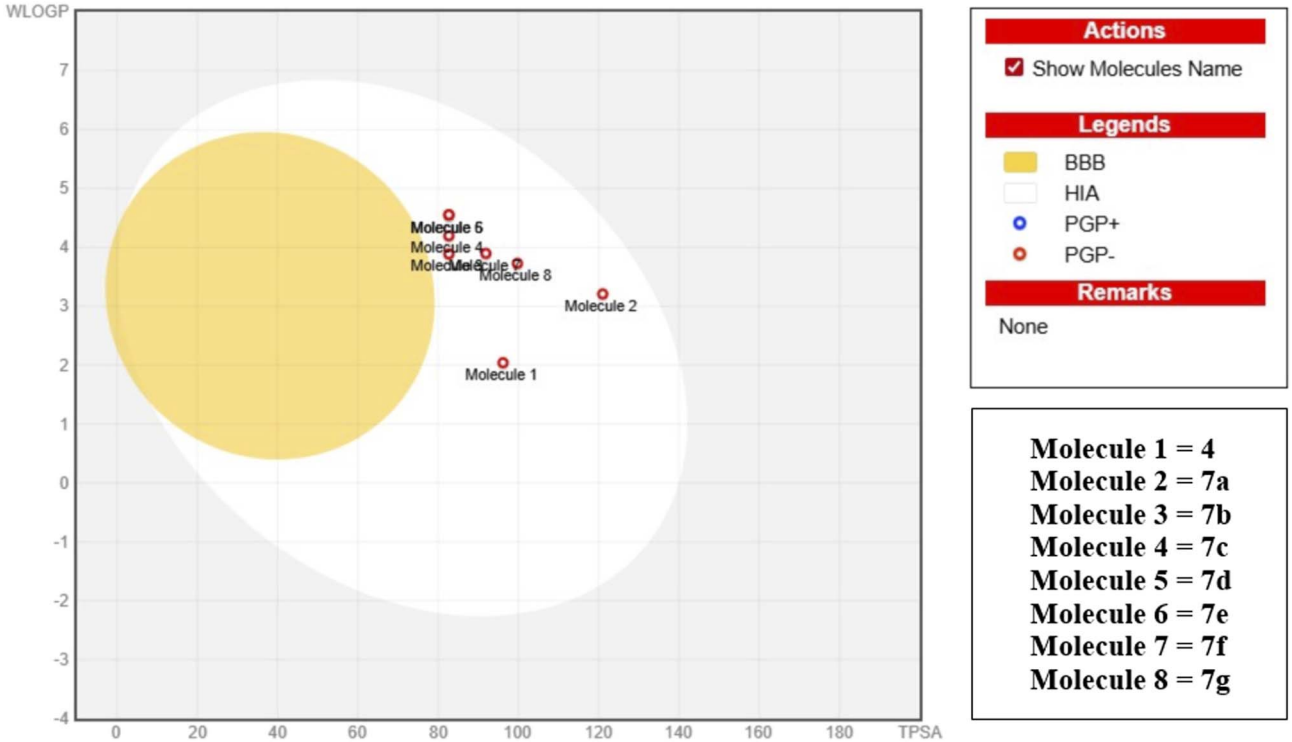

Fig. 10 Boiled egg image of the oxadiazole derivatives (**4**, **7a–7g**).

Compound **4** was notably simple, exhibited good solubility, and demonstrated drug-like characteristics, making it an excellent lead compound. The **7a–7g** series of compounds, while slightly more complex, also exhibited a favorable balance of lipophilicity, solubility, flexibility, and bioavailability. Their exceptional performance across multiple drug-likeness criteria, low toxicity risks, and manageable synthetic accessibility render them promising candidates for further optimization and development.

The BOILED-Egg model in Fig. 10 is a graphical tool used to predict the absorption and blood–brain barrier (BBB) permeability of molecules based on two key properties: WLOGP, which represents lipophilicity, and TPSA, which measures the polarity. The BOILED-Egg model offered a lucid visual depiction of the absorption potential and brain penetration capability of oxadiazole molecules **1–8** (*i.e.*, **4**, **7a–7g**, respectively). The findings suggest that the majority of the molecules in the dataset are appropriate for oral drug development, as they are located within the HIA region.

However, this also meant that only a very few of the molecules possessed the appropriate properties to cross the BBB; hence, they might not have been effectively used for CNS-related applications. The presence of non-PGP substrate molecules was desirable because these compounds should have exhibited lower values in the active pumping out of the cells, leading to overall improved permeability.

The spiderweb plot for compounds **4**, **7a–7g** in Fig. S11 (SI), (A) to (H), illustrates various physicochemical properties. The six axes in the graph are attributed to different molecular characteristics: lipophilicity (LIPO), molecular size (SIZE), polarity (POLAR), insolubility (INSOLU), unsaturation (INSATU), and molecular flexibility (FLEX). The red line represents the connection between the data points for **4**, **7a–7g**, providing a graphical representation of its molecular profile. All the parameters for compound **4** are within the limit except for FLEX, which is slightly low, indicating a rigid structure, and a slightly higher INSATU, indicating more double bonds, which also resulted in compound rigidity.

The spiderweb plot for compound **7a** depicted six critical molecular properties, all of which were within the acceptable range. Notably, the FLEX parameter indicated a moderately high capacity for the molecule to adopt various conformations, thereby enhancing its adaptability in binding interactions. In contrast, the spiderweb plots for compounds **7b–7g** revealed six significant molecular properties that characterize their chemical and biological behavior. All properties were within favorable limits, except for unsaturation (INSATU), which indicated a slightly higher degree of double bonding. This increased molecular rigidity could potentially contribute to stronger binding affinities.

3. Experimental

3.1. General

All reagents and chemicals utilized in this study were obtained from Sigma Aldrich and BDH and employed without further purification. The melting points of the compounds were determined using an M-560 Buchi melting point apparatus. The

infrared (IR) spectra of the compounds were recorded using a Fourier-transform infrared (FTIR) spectrophotometer (PerkinElmer, USA). A Bruker Avance III spectrophotometer was employed to record the ^{1}H- and ^{13}C-NMR spectra at 400 and 100 MHz, respectively. The chemical shift values were measured in parts per million (ppm), while the coupling constant J values were recorded in hertz (Hz).

3.2. Procedure for synthesis of 5-(3,4-dimethoxyphenyl)-1,3,4-oxadiazole-2-thiol (4)

In a round-bottomed (RB) flask, 1 mmol (0.1822 g) of 3,4-dimethoxybenzoic acid **1** was added to 20 mL of dry methanol, followed by the addition of a few drops of concentrated H_2SO_4. The reaction mixture was stirred at reflux temperature for 5–6 hours to obtain the desired ester **2**. The progress of the reaction was monitored by thin-layer chromatography (TLC) in a 50% polar solvent system of ethyl acetate and *n*-hexane. After completion of the reaction, the mixture was allowed to cool, and sodium bicarbonate solution was added to neutralize the unreacted sulfuric acid. Methyl ester was extracted from the mixture using ethyl acetate (20 mL × 3), and the solvent was evaporated using a rotary evaporator to obtain the ester. The ester was dissolved in 10 mL of dry methanol, followed by the addition of hydrazine hydrate, and it was refluxed under constant stirring for 4–5 hours to afford hydrazide **3**. The reaction progress was checked by TLC, and after completion of reaction, the mixture was poured into cold distilled water. The precipitates that appeared were filtered, thoroughly washed with water, dried overnight, and collected.

In the next step, hydrazide **3** was dissolved in 50 mL of dry methanol, and KOH was added to the mixture, followed by the slow addition of CS_2 (20 mmol) to synthesize intermediate oxadiazole **4**. The reaction mixture was refluxed for 15–16 hours, and progress was monitored by TLC. After completion, the mixture was decanted into a beaker containing cold distilled water and neutralized using an aqueous HCl solution. Crude oxadiazole **4** appeared as precipitates, which were filtered, washed, and recrystallized with methanol to obtain pure oxadiazole **4** for further reactions.

3.3. Synthesis of 2-bromo-*N*-substituted acetamide (6a)

In a typical reaction, amine (1-amino-2-(4-methoxyphenyl) ethane) was dissolved in 20 mL dichloromethane (DCM) containing a catalytic amount of triethylamine, followed by the addition of 2-bromoacetyl bromide (5 mmol). The reaction mixture was stirred at 0 °C for 5–6 hours, and the progress was monitored using TLC. The mixture was then poured into a beaker containing cold distilled water. Compound **6a** was extracted using ethyl acetate to obtain the desired acetamide, which was purified by recrystallization from ethanol.

3.4. Procedure for the synthesis of *S*-substituted oxadiazole derivatives (7a–7g)

S-Substituted 1,3,4-oxadiazole derivatives **7a–7g** were synthesized by refluxing compound **4** with various aromatic halides (**6a–6g**). In a typical reaction, 2-mercapto-1,3,4-oxadiazole was dissolved in 20 mL of acetone, followed by the addition of K_2CO_3, followed by the addition of various aromatic halides (**6a–6g**). The reaction mixture was refluxed for 9–10 hours. The progress of the reaction was confirmed by TLC, after which the mixture was poured into cold water. The precipitates appeared were filtered, washed and final products were purified by column chromatography using *n*-hexane and ethyl acetate as eluents with gradient elution. The structures of these derivatives were confirmed by state-of-the-art spectroscopic methods (FT-IR, ^{1}H-, and ^{13}C-NMR) as depicted in Fig. S12–S19 (SI).

3.4.1. 5-(3,4-Dimethoxyphenyl)-1,3,4-oxadiazole-2-thiol (4). Yellow solid: yield 82%: m.p. 243 °C: FTIR (ATR, ν_{max} cm^{-1}), 3245 (S–H stretching), 2961 (aromatic, C–H), 2836 (alkyl, C–H stretching), 1623 (aromatic C=C bending), 1611 and 1477 (aromatic 1,3,4-oxadiazole stretching), 1249 and 1171 (aromatic C–O–C stretching): ^{1}H NMR (400 MHz, DMSO, ppm) δ 7.48 (d, J = 8.0 Hz, 1H, H-3′), 7.34 (s, J = 2.0 Hz, 1H, H-1′), 7.15 (d, J = 8.0 Hz, 1H, H-2′), 3.85 (s, 6H, –OCH$_3$), 3.35 (s, 1H, –SH): ^{13}C NMR (101 MHz, DMSO, ppm) δ 177.1 (C-1), 160.6 (C-2), 152.1 (C-5′), 149.1 (C-3′), 119.7 (C-4′), 114.6 (C-1′), 112.0 (C-6′), 108.5 (C-2′), 55.7 (–OCH$_3$); anal calcd for $C_{10}H_{10}N_2O_3S$: C, 50.42; H, 4.20; N, 11.76 found C, 50.35; H, 4.12; N, 11.71.

3.4.2. 2-((5-(3,4-Dimethoxyphenyl)-1,3,4-oxadiazol-2-yl) thio)-*N*-(4-methoxyphenethyl)acetamide (7a). Light yellow solid: yield 72%: m.p. 129 °C: FTIR (ATR, ν_{max} cm^{-1}) 3225 (amide, N–H stretching), 2995 (aromatic, C–H stretch), 2833 (alkyl, C–H stretching), 1723 (C=O), 1643 (aromatic C=C), 1228 and 1174 (aromatic C–O–C stretching), 699 (C–S stretch): ^{1}H NMR (400 MHz, DMSO, ppm) δ 10.79 (s, 1H, –NH–″), 7.51 (d, J = 8.0 Hz, 1H, H-3′), 7.48 (s, 1H, H-1′) 7.18 (d, J = 8.0 Hz, 1H, H-2′), 7.06 (d, J = 8.0 Hz, 2H, H-1″,3″), 6.86 (d, J = 8.0 Hz, 2H, H-2″,4″), 3.96 (m, 2H, –CH$_2$–), 3.88 (m, 2H, –CH$_2$–), 3.82 (s, 6H, –OCH$_3$), 3.72 (s, 3H, –OCH$_3$), 2.92 (s, 2H, –CH$_2$–): ^{13}C NMR (101 MHz, DMSO, ppm) δ 171.3 (C-1), 162.9 (C-2), 157.9 (C=O), 151.4 (C-5′), 148.3 (C-3′), 129.9 (C-4″), 129.7 (C-2″,6″), 125.5 (C-1″), 120.6 (C-4′), 113.8 (C-1′), 113.7 (C-3″,5″), 111.0 (C-6′), 110.6 (C-2′), 55.6 (–OCH$_3$), 54.9 (–OCH$_3$), 43.9 (–CH$_2$–), 32.3 (–CH$_2$–), 31.1 (–CH$_2$–); anal calcd for $C_{21}H_{23}N_3O_5S$: C, 58.74; H, 5.36; N, 9.79 found C, 58.67; H, 5.28; N, 9.73.

3.4.3. 2-(Benzylthio)-5-(3,4-dimethoxyphenyl)-1,3,4-oxadiazole (7b). Light yellow solid: yield 94%: m.p. 102 °C: FTIR (ATR, ν_{max} cm^{-1}) 2968 cm^{-1} (aromatic, C–H stretch), 2836 (alkyl, C–H), 1607 (aromatic C=C), 1233 (aromatic C–O–C): ^{1}H NMR (400 MHz, DMSO, ppm) δ 7.55–7.49 (m, 1H, H-3′), 7.50–7.44 (m, 2H, H-2″,4″), 7.44–7.38 (m, 1H, H-1′), 7.38–7.24 (m, 3H, H-1″,3″,5″), 7.13 (m, 1H, H-2′), 4.56 (s, 2H, –CH$_2$–), 3.84 (s, 6H, –OCH$_3$): ^{13}C NMR (101 MHz, DMSO, ppm) δ 165.2 (C-1), 162.4 (C-2), 151.8 (C-5′), 149.0 (C-3′), 136.6 (C-1″), 129.0 (C-3″,5″), 128.5 (C-2″,6″), 127.7 (C-4″), 119.9 (C-4′), 115.2 (C-1′), 111.9 (C-6′), 108.9 (C-2′), 55.7 (–OCH$_3$′), 35.9 (–CH$_2$–); anal calcd for $C_{17}H_{16}N_2O_3S$: C, 62.19; H, 4.87; N, 8.53 found C, 62.13; H, 4.83 N, 8.46.

3.4.4. 2-(3,4-Dimethoxyphenyl)-5-((2-methylbenzyl)thio)-1,3,4-oxadiazole (7c). Yellow solid: yield 95%: m.p. 87 °C: FTIR (ATR, ν_{max} cm^{-1}) 3078 cm^{-1} (aromatic, C–H stretching), 2840 (alkyl, C–H), 1610 (aromatic C=C), 1597 (C=N), 1230 and 1170 cm^{-1} (aromatic C–O–C stretching), 682 (C–S): ^{1}H NMR

(400 MHz, DMSO, ppm) δ 7.54 (d, J = 8.0 Hz, 1H, H-3′), 7.43 (s, 1H, H-2″,5″), 7.39 (d, J = 8.0 Hz, 1H, H-1′), 7.22 (s, 2H, H-3″,4″), 7.15 (d, J = 8.0 Hz, 2H, H-2′), 4.58 (s, 2H, –CH_2–), 3.85 (s, 6H, –OCH_3), 2.40 (s, 3H, –CH_3): ^{13}C NMR (101 MHz, DMSO, ppm) δ 165.3 (C-1), 162.3 (C-2), 151.9 (C-5′), 149.1 (C-3′), 136.8 (C-1″), 133.9 (C-2″), 130.5 (C-4″), 130.0 (C-5″), 128.2 (C-6″), 126.1 (C-3″), 120.0 (C-4′), 115.2 (C-1′), 112.0 (C-6′), 109.0 (C-2′), 55.7 (–OCH_3′), 34.5 (–CH_2–), 18.7 (–CH_3); anal calcd for $C_{18}H_{18}N_2O_3S$: C, 63.15; H, 5.26; N, 8.18 found C, 63.10; H, 5.21 N, 8.11.

3.4.5. 2-((2-Chlorobenzyl)thio)-5-(3,4-dimethoxyphenyl)-1,3,4-oxadiazole (7d). Greenish yellow solid: yield 65%: m.p. 74 °C: FTIR (ATR, ν_{max} cm^{-1}) 2995 (aromatic, C–H), 2830 (alkyl, C–H), 1609 (aromatic C=C), 1597 (C=N), 1235 (aromatic C–O–C), 685 (C–S): ^{1}H NMR (400 MHz, DMSO, ppm) δ 7.61 (d, J = 8.0 Hz, 1H, H-3′), 7.51 (t, J = 8.0, 2H, H-3″,4″), 7.40 (d, J = 8.0 Hz, 1H, H-1′), 7.34 (t, J = 8.0, 2H, H-2″,5″), 7.14 (d, J = 8.0 Hz, 1H, H-2′), 4.62 (s, 2H, –CH_2–), 3.84 (s, 6H, –OCH_3): ^{13}C NMR (101 MHz, DMSO, ppm) δ 166.0 (C-1), 162.4 (C-2), 152.3 (C-5′), 149.5 (C-3′), 134.4 (C-2″), 133.7 (C-1″), 132.0 (C-4″), 130.4 (C-5″), 130.1 (C-6″), 127.9 (C-3″), 120.4 (C-4′), 115.6 (C-1′), 112.4 (C-6′), 109.4 (C-2′), 56.1 (–OCH_3), 34.7 (–CH_2–); anal calcd for $C_{17}H_{15}N_2ClO_3S$: C, 56.27; H, 4.13; N, 7.72 found C, 56.22; H, 4.08 N, 7.67.

3.4.6. 2-((4-Chlorobenzyl)thio)-5-(3,4-dimethoxyphenyl)-1,3,4-oxadiazole (7e). Yellow solid: yield 75%: m.p. 78 °C: FTIR (ATR, ν_{max} cm^{-1}) 2955 (aromatic, C–H), 2832 cm^{-1} (alkyl, C–H), 1608 (aromatic C=C), 1596 (C=N), 1240 (aromatic C–O–C), 690 (C–S): ^{1}H NMR (400 MHz, DMSO, ppm) δ 7.51 (d, J = 8.0, 2H, H-2″,4″), 7.50 (d, J = 8.0, 1H, H-3′), 7.41 (d, J = 8.0, 2H, H-1″,5″), 7.40 (s, 1H, H-1′), 7.14 (d, J = 8.0, 1H, H-2′), 4.56 (s, 2H, –CH_2–), 3.84 (s, 6H, –OCH_3′): ^{13}C NMR (101 MHz, DMSO, ppm) δ 165.8 (C-1), 162.8 (C-2), 152.3 (C-5′), 149.5 (C-3′), 136.5 (C-1″), 132.8 (C-4″),131.6 (C-2″,6″), 129.0 (C-3″,5″), 120.4 (C-4′), 115.6 (C-1′), 112.4 (C-6′), 109.3 (C-2′), 56.1 (–OCH_3′), 35.5 (–CH_2–); anal calcd for $C_{17}H_{15}N_2ClO_3S$: C, 56.27; H, 4.13; N, 7.72 found C, 56.22; H, 4.08 N, 7.67.

3.4.7. 2-(3,4-Dimethoxyphenyl)-5-((3-methoxybenzyl)thio)-1,3,4-oxadiazole (7f). Light brown solid: yield 62%: m.p. 106 °C: FTIR (ATR, ν_{max} cm^{-1}) 2950 (aromatic, C–H stretching), 2839 (alkyl, C–H stretching), 1607 (aromatic C=C), 1583 (C=N), 1233 (aromatic C–O–C), 685 (C–S): ^{1}H NMR (400 MHz, DMSO, ppm) δ 7.52 (t, J = 8.0 Hz, 1H, H-3′), 7.40 (d, J = 8.0 Hz, 1H, H-1′), 7.25 (t, J = 8.0 Hz, 1H, H-4″), 7.12 (d, J = 8.0 Hz, 1H, H-2′), 7.03 (d, J = 8.0 Hz, 2H, H-3″,5″), 6.84 (t, J = 8.0 Hz, 1H, H-1″), 4.51 (distorted AB q, 2H, –CH_2–″), 3.82 (s, 6H, –OCH_3′), 3.71 (s, 3H, –OCH_3″): ^{13}C NMR (101 MHz, DMSO, ppm) δ 165.3 (C-1), 162.5 (C-2), 159.2 (C-5″), 151.9 (C-5′), 149.1 (C-3′), 138.1 (C-1″), 129.6 (C-3″), 121.1 (C-6″), 119.9 (C-4′), 115.2 (C-1′), 114.6 (C-4″), 113.2 (C-2″), 112.0 (C-6′), 109.0 (C-2′), 55.7 (3′-OCH_3), 55.0 (–OCH_3), 35.9 (–CH_2–); anal calcd for $C_{18}H_{18}N_2O_4S$: C, 60.33; H, 5.02; N, 7.82 found C, 60.28; H, 4.97 N, 7.77.

3.4.8. 2-((5-(3,4-Dimethoxyphenyl)-1,3,4-oxadiazol-2-yl) thio)-1-phenylethan-1-one (7g). Yellowish brown solid: yield 74%: m.p. 166 °C: FTIR (ATR, ν_{max} cm^{-1}) 3343 (enol, –OH, stretching), 3072 (alkenyl, C–H stretching), 3001 cm^{-1} (aromatic, C–H), 2837 (alkyl, C–H), 1679 (carbonyl, C=O), 1608 (aromatic C=C), 1596 (C=N), 1232 (aromatic C–O–C), 682 (C–S): ^{1}H NMR (400 MHz, DMSO, ppm) δ 8.07 (d, J = 7.6 Hz, 2H, H-1″,5″), 7.72 (t, J = 8.0 Hz, 1H, H-3″), 7.59 (t, J = 8.0 Hz, 2H, H-2″,4″), 7.52 (d, J = 8.0 Hz, 1H, H-3′), 7.39 (s, 1H, H-1′), 7.13 (d, J = 8.0 Hz, 1H, H-2′), 5.17 (s, 2H, –CH_2–″), 3.82 (s, 6H, –OCH_3′): ^{13}C NMR (101 MHz, DMSO, ppm) δ 192.7 (C=O), 165.1 (C-1), 162.5 (C-2), 151.8 (C-5′), 149.0 (C-3′), 135.0 (C-1″), 134.0 (C-4″), 128.9 (C-3″,5″), 128.5 (C-2″,6″), 119.9 (C-4′), 115.2 (C-1′), 112.0 (C-6′), 108.9 (C-2′), 55.7 (–OCH_3), 55.6 (–OCH_3), 40.5 (–CH_2–); anal calcd for $C_{18}H_{16}N_2O_4S$: C, 60.67; H, 4.49; N, 7.86 found C, 60.62; H, 4.43 N, 7.81.

3.5. Ecto-NTPDase inhibition activity

Enzyme preparation of recombinant NTPDase1–3 and 8 was performed according to the previously reported method.[25] The assay was performed with recombinant human NTPDases (h-NTPDase1–3 and 8) by slightly amending the previously reported method.[26] Enzymatic reactions were carried out in an incubation medium with a pH of 7.4, consisting of Tris–HCl in combination with $CaCl_2$ at concentrations of 50 mM and 5 mM. Initially, the synthesized 1,3,4-oxadiazole derivatives **4** and **7a–7g** were screened at 100 μM, and the final %v/v concentration of DMSO was maintained at 1%. The reaction mixture containing the buffer (55 μL), 10 μL of test compound solution, and 10 μL of enzyme preparation was pre-incubated at 37 °C (10 min). The enzyme preparations were used at the following concentration (per well): 59 ng for h-NTPDase1, 43 ng for NTPDase2, 105 ng for NTPDase3, and 89 ng for NTPDase8. A 15 minutes incubation was carried out at 37 °C after the careful addition of the 100 μM, 10 μL solution of ATP as substrate with concentration (0.5, 1.0 and 2.0 mM) to begin the reaction. Finally, the reaction was completed by adding malachite green reagent having a concentration of 15 μL, and free inorganic phosphate was detected by measuring the absorbance at 630 nm using a microplate reader (BioTek ELx800 Instruments, Inc., Vermont, USA). All experiments and measurements were performed in triplicate. The oxadiazoles displaying >50% inhibition of any isozyme of h-NTPDase were diluted again and their concentration–inhibition curves were obtained. Data were analyzed, and IC_{50} values were measured using PRISM 5.0 (GraphPad, California, USA).

3.6. Enzyme inhibitory kinetics

Inhibitory kinetic studies were performed to determine the type of inhibition and the K_m values of the enzyme–substrate complex. Experiments were similar to the inhibition assay except for four different concentrations of the best inhibitor **7g**, *i.e.*, 0, 2.5, 5.0, 10.0 μM against NTPDase1; 0, 5.0, 10.0, 15.0 μM against NTPDase2; 0, 0.60, 1.20, 2.4 μM against NTPDase3, and 0, 7.5, 15.0, 30.0 μM against NTPDase8 were taken, and Lineweaver–Burk plots were drawn using Graph Pad Prism Software.

3.7. Computational studies for MEP and chemical reactivity

The molecular electrostatic surface potential (MEP) and the energies of the highest occupied molecular orbital (HOMO) and lowest unoccupied molecular orbital (LUMO), and dipole moments for the 1,3,4-oxadiazoles with the best docking scores and IC_{50} values against ecto-NTPDases were evaluated using

Gaussian 16 software at the DFT/6-31G(d,p)/B3LYP level of theory.[27]

3.8. Docking studies and homology modelling of NTPDase8

Three PDB files with IDs 4BRQ, 4BR5, and 4A59 for NTPDases 1, 2, and 3,[28–30] respectively, and their docked ligands in SDF files were downloaded directly from the https://www.rcsb.org/ website. NTPDase8 was obtained by acquiring a sequence of amino acids for human NTPDase8 from the UNIPROT database and running it on the SWISS modelling server for homology modelling.[31,32]

The PDB files were analyzed using Biovia Discovery Studio 2024 software, and the entrance channels of co-crystallized ligands along with the amino acid residues interacting with these ligands were determined.[33] Biovia Discovery Studio 2024 software was also used to generate a library of selected ligands, including the crystallized ligands (except for NTPDase8) present in the PDB files for docking studies. The docking scores were evaluated using Maestro 12.5, Schrodinger 2020-3. The selected ligands were optimized using the Ligprep module with default settings using Epik and OPLS3e force fields, and allowed to generate one optimized structure per ligand. The PDB files of NTPDase1–3 and 8 were prepared by protein preparation using default settings and deleting the chains of amino acids, if present, containing identical co-crystallized ligands, except chain A for each enzyme, during the review and modification step. Receptor grid was generated before closing the protein preparation wizard, employing the centroid of workspace ligand or providing the ligand coordinates obtained from PDB 3CJ9 for the homology model of NTPDase8, and using default settings except for the size of ligands, which was kept at 20 Å. Docking was performed using the ligand-docking module, uploading the receptor grid, and optimized ligand files. Extra precision method was chosen for docking, and the amino acid residues of binding pocket obtained from the analysis of each PDB file were specified, except for NTPDase8, where a 20 Å grid space for the ligands was selected.

3.9. Structural interaction fingerprint (SIFt) analysis

Following the execution of computational molecular docking studies, Structural Interaction Fingerprint (SIFt) module available in Maestro 12.5, Schrodinger 2020-3, was employed to assess the amino acid residues and water molecule-mediated interactions present among ecto-NTPDases and 1,3,4-oxadiazoles, as well as the redocked standards **Amp** and **Anp**. This analysis yielded significant insights into binding interactions and docking scores of the compounds and redocked standards.

3.10. *In silico* pharmacokinetic studies

Pharmacokinetic parameters such as absorption, distribution, metabolism, excretion, and toxicity (ADME/T), were evaluated using two different tools: pkCSM and SwissADME.[34,35] pkCSM tool was used to evaluate the pharmacokinetic properties of chemical compounds by analyzing various parameters related to absorption, distribution, metabolism, excretion, and toxicity (ADME/T). By utilizing pkCSM, important insights were obtained into the pharmacokinetic behavior and potential safety concerns of compounds from Scheme 1, aiding in drug development and risk assessment. SwissADME tool was used to evaluate the ADME parameters of selected ligands. A heat map, boiled egg image, and spiderweb plots were generated for the synthesized 1,3,4-oxadiazole derivatives to provide decisive insights into the various pharmacokinetic properties.

4. Conclusions

Present study elucidates the inhibitory potential of synthesized 1,3,4-oxadiazole derivatives (**4**, **7a–7g**) against ecto-NTPDases, with a particular focus on NTPDase2, which is implicated in tumorigenesis and cancer progression. The structural integrity of synthesized heterocycles was confirmed through spectral data, including FTIR, ^{1}H, and ^{13}C NMR. Pharmacokinetic analysis revealed that all derivatives exhibited a favorable safety profile, with minimal or no pharmacokinetic violations. Molecular docking studies demonstrated significant inhibition of the target enzyme ecto-NTPDase, characterized by high binding affinities and stable interactions within the active site. Validation of docking scores using SIFt analysis indicated that water-mediated interactions contributed to the superior docking scores of standard inhibitors compared to 1,3,4-oxadiazoles. DFT calculations corroborated the stability and electronic suitability of the best-docked hits and *in vitro* inhibition. *In vitro* ecto-NTPDase inhibition assays yielded promising results, particularly for compound **7g**, which emerged as the most potent inhibitor due to its bonding and non-bonding interactions, as confirmed by structure–activity relationship (SAR) analysis. Compounds **7d** and **7c** also demonstrated notable inhibition of NTPDase3 and NTPDase8, respectively. The inhibitory kinetics of **7g** against NTPDase1 and 2 revealed non-competitive inhibition with low K_m values, indicating strong binding affinities, whereas against NTPDase3 and 8, **7g** exhibited mixed-type inhibition with varying K_m values. Increase in K_m suggested the substrate's inability to bind to the enzyme–inhibitor complex and *vice versa*. This study provides substantial evidence that 1,3,4-oxadiazoles could serve as effective lead structures for developing novel anticancer agents targeting ecto-NTPDases, particularly NTPDase2, thereby offering a promising avenue for future therapeutic exploration.

Author contributions

Conceptualization, Z. A., and M. L.; methodology, S. Z. A., K. S., and S. R.; software, S. Z. A., and M. A. R.; validation of study, S. R., M. A., K. S., S. A., S. Z. A., and I. S.; formal analysis, Z. A., M. L., M. A., and K. S.; investigation, Z. A., and M. A. R.; resources, Z. A., S. A., and M. L.; data curation, S. R., M. A. R., and S. A.; writing-original draft preparation, S. R., S. Z. A., I. S., Z. A., and M. L.; writing-review and editing, M. A. R., Z. A., I. S., K. S., and M. L.; visualization, K. S., M. A. R., Z. A., and M. L.; supervision, M. L., and Z. A.; project administration, M. L., and Z. A.; funding acquisition, I. S., and Z. A. All authors have read and agreed to the published version of the manuscript.

Conflicts of interest

The authors declared no conflict of interest.

Data availability

Upon request, data could be provided by the shared corresponding author.

Supplementary information (SI) is available. See DOI: https://doi.org/10.1039/d6ra01543c.

Acknowledgements

The authors extend their appreciation to the Deanship of Scientific Research, Islamic University of Madinah, Saudi Arabia, for funding this research work. In addition, the authors extend their profound appreciation to the Higher Education Commission of Pakistan for providing partial assistance which enabled the completion of this research.

References

1 W. Chen and G. Guidotti, Soluble apyrases release ADP during ATP hydrolysis, *Biochem. Biophys. Res. Commun.*, 2001, **282**(1), 90–95.
2 P. Heine, *et al.*, Functional characterization of rat ecto-ATPase and ecto-ATP diphosphohydrolase after heterologous expression in CHO cells, *Eur. J. Biochem.*, 1999, **262**(1), 102–107.
3 F. Kukulski, *et al.*, Comparative hydrolysis of P2 receptor agonists by NTPDases 1, 2, 3, and 8, *Purinergic Signal.*, 2005, **1**(2), 193–204.
4 B. P. Chadwick and A.-M. Frischauf, The CD39-like Gene Family: Identification of Three New Human Members (CD39L2, CD39L3, and CD39L4), Their Murine Homologues, and a Member of the Gene Family From Drosophila Melanogaster, *Genomics*, 1998, **50**(3), 357–367.
5 B. Kege, *et al.*, An ecto-ATPase and an ecto-ATP diphosphohydrolase are expressed in rat brain, *Neuropharmacology*, 1997, **36**(9), 1189–1200.
6 S. M. Vlajkovic, *et al.*, Evidence for alternative splicing of ecto-ATPase associated with termination of purinergic transmission, *Mol. Brain Res.*, 1999, **73**(1–2), 85–92.
7 A. F. Knowles and W.-C. Chiang, Enzymatic and transcriptional regulation of human ecto-ATPase/E-NTPDase2, *Arch. Biochem. Biophys.*, 2003, **418**(2), 217–227.
8 L. Gao, L. Dong and J. P. Whitlock, A novel response to dioxin: induction of ecto-ATPase gene expression, *J. Biol. Chem.*, 1998, **273**(25), 15358–15365.
9 A. F. Knowles, Differential expression of ectoMg2+-ATPase and ectoCa2+-ATPase activities in human hepatoma cells, *Arch. Biochem. Biophys.*, 1988, **263**(2), 264–271.
10 M. Al-Rashida, *et al.*, Ectonucleotidase inhibitors: a patent review (2011-2016), *Expert Opin. Ther. Pat.*, 2017, **27**(12), 1291–1304.
11 T. Khamkar, *et al.*, Recent Advances in Synthetic Approaches for 1, 3, 4-Oxadiazole Derivatives: A Comprehensive Review on Therapeutic Applications, *Open Med. Chem. J.*, 2025, **19**(1), 1–16.
12 G. M. Amle, Cutting-Edge Developments in 1, 3, 4-Oxadiazole Derivatives: Synthesis, Properties, and Applications, *Int. J. Sci. Res. Sci. Technol.*, 2025, **12**(7), 196–199.
13 S. S. Mishra, *et al.*, Unveiling the Anti-cancer Potential of Oxadiazole Derivatives: A Comprehensive Exploration of Structure-Activity Relationships and Chemico-Biological Insights, *Med. Chem.*, 2025, **21**(6), 445–470.
14 A. I. Qazi, *et al.*, Evaluation of antidiabetic activity of oxadiazole derivative in rats, *Evid. Based Complement. Alternat. Med.*, 2023, **2023**(1), 1141554.
15 T. Glomb and P. Świątek, Antimicrobial activity of 1, 3, 4-oxadiazole derivatives, *Int. J. Mol. Sci.*, 2021, **22**(13), 6979.
16 A. Almasirad, *et al.*, Synthesis, analgesic and anti-inflammatory activities of new methyl-imidazolyl-1, 3, 4-oxadiazoles and 1, 2, 4-triazoles, *Daru, J. Pharm. Sci.*, 2014, **22**(1), 22.
17 S. M. Rana, *et al.*, Synthesis, computational studies, antioxidant and anti-inflammatory bio-evaluation of 2, 5-disubstituted-1, 3, 4-oxadiazole derivatives, *Pharmaceuticals*, 2023, **16**(7), 1045.
18 D. G. Shiferaw and B. Kalluraya, Synthesis, characterization, biological evaluation, and molecular docking studies of new 1, 3, 4-oxadiazole-thioether derivative as antioxidants and cytotoxic agents, *Heliyon*, 2024, **10**(7), e28634.
19 S. Gandamalla, *et al.*, Substituted 1, 3, 4-oxadiazole coupled 1, 2, 3-triazole derivatives as antiproliferative agents: design, synthesis, biological evaluation and *in silico* studies, *J. Chin. Chem. Soc.*, 2025, **72**(6), 721–738.
20 Q. Wu, *et al.*, Activity of GPCR-targeted drugs influenced by human gut microbiota metabolism, *Nat. Chem.*, 2025, 1–14.
21 R. Palit, N. Saraswat and J. Sahoo, Review on substituted 1, 3, 4-oxadiazole and its biological activities, *Int. Res. J. Pharm.*, 2016, **7**(2), 1–7.
22 V. Hegde, *et al.*, Discovery of Novel Oxadiazole-Triazole Hybrids as Lung and Cervical Cancer Agents: Synthesis, Docking, Biological Evaluation, and SAR Studies, *Chem. Biol. Drug Des.*, 2025, **106**(6), e70225.
23 Y. Zhang, *et al.*, Synthesis and Antibacterial Activities of 2-(1-Aryl-5-Methyl-1, 2, 3-triazol-4-yl)-1, 3, 4-Oxadiazole Derivatives, *J. Chin. Chem. Soc.*, 2002, **49**(3), 369–373.
24 M. B. Patel, *et al.*, Calix [4] arene based 1, 3, 4-oxadiazole and thiadiazole derivatives: Design, synthesis, and biological evaluation, *Org. Biomol. Chem.*, 2012, **10**(9), 1785–1794.
25 M. Martín-Satué, *et al.*, Localization of plasma membrane bound NTPDases in the murine reproductive tract, *Histochem. Cell Biol.*, 2009, **131**(5), 615–628.
26 J. Sévigny, *et al.*, Differential catalytic properties and vascular topography of murine nucleoside triphosphate diphosphohydrolase 1 (NTPDase1) and NTPDase2 have implications for thromboregulation, *Blood*, 2002, **99**(8), 2801–2809.
27 M. E. Frisch, *et al.*, *Gaussian 16*, Gaussian, Inc., Wallingford, CT, 2016.

28 J. P. Vivian, *et al.*, Crystal structure of a Legionella pneumophila ecto-triphosphate diphosphohydrolase, a structural and functional homolog of the eukaryotic NTPDases, *Structure*, 2010, **18**(2), 228–238.
29 M. Zebisch, *et al.*, Crystallographic snapshots along the reaction pathway of nucleoside triphosphate diphosphohydrolases, *Structure*, 2013, **21**(8), 1460–1475.
30 U. Krug, *et al.*, Structural insight into activation mechanism of Toxoplasma gondii nucleoside triphosphate diphosphohydrolases by disulfide reduction, *J. Biol. Chem.*, 2012, **287**(5), 3051–3066.
31 S. Ahmad, *et al.*, The UniProt website API: facilitating programmatic access to protein knowledge, *Nucleic Acids Res.*, 2025, gkaf394.
32 A. Waterhouse, *et al.*, SWISS-MODEL: homology modelling of protein structures and complexes, *Nucleic Acids Res.*, 2018, **46**(W1), W296–W303.
33 BIOVIA Discovery Studio, *Dassault Systèmes*, Dassault Systèmes, San Diego, 2024, https://www.3ds.com/products/biovia.
34 D. E. Pires, T. L. Blundell and D. B. Ascher, pkCSM: predicting small-molecule pharmacokinetic and toxicity properties using graph-based signatures, *J. Med. Chem.*, 2015, **58**(9), 4066–4072.
35 A. Daina, O. Michielin and V. Zoete, SwissADME: a free web tool to evaluate pharmacokinetics, drug-likeness and medicinal chemistry friendliness of small molecules, *Sci. Rep.*, 2017, **7**(1), 42717.